Journal of Aircraft, Available online 13 February 2025
DOI:10.2514/1.c037894

Potential for Energy Recovery of a Non-Adiabatic Subsonic Airfoil

Joseph E. Lister-Symonds,[*] Ngonidzashe E. Mutangara,[†]
Ioannis Lamprakis,[‡] and Drewan S. Sanders.[§]
Cranfield University, Cranfield, Bedfordshire, England MK43 0AL, United Kingdom

This paper investigates the effect of wall temperature and flow conditions on the Potential for Energy Recovery of the NACA0012 airfoil. A work-energy balance has been derived from the governing equations for moving control volumes for a body in dynamic equilibrium, aerodynamically decoupled from its propulsive source. The formulation has been applied to an extensive test matrix of computational fluid dynamics cases, with steady level flight imposed and wall temperature, angle of attack, Reynolds and Mach number varied independently. The decomposition of the wake energy shows explicitly that the near-field work of the body manifests as global energy constituents, viscous dissipation and baroclinic work. The analysis identifies the conditions and underlying mechanisms which minimize and maximize the Potential for Energy Recovery, revealing that there are synergistic opportunities for tightly coupled airframe and propulsor configurations with waste heat to reject.

Nomenclature

a	=	speed of sound [m/s]
c	=	airfoil chord length [m]
C_D	=	drag force coefficient [-]
C_{DV}	=	non-dimensional drag power [-]
C_L	=	lift force coefficient [-]
c_p	=	isobaric heat capacity [J/kg/K]

[*] Postgraduate, Centre for Propulsion and Thermal Power Engineering, joe.listersymonds@gmail.com
[†] Ph.D. Researcher, Centre for Propulsion and Thermal Power Engineering, ngonidzashe.e.mutangara@cranfield.ac.uk
[‡] Ph.D. Researcher, Centre for Propulsion and Thermal Power Engineering
[§] Lecturer, Centre for Propulsion and Thermal Power Engineering, d.s.sanders@cranfield.ac.uk

C_p	=	pressure coefficient [-]
d	=	distance [m]
D	=	drag force [N]
$\mathrm{d}\mathcal{S}$	=	infinitesimal surface area [m^2]
$\mathrm{d}\mathcal{V}$	=	infinitesimal volume [m^3]
e_a^{21}	=	mesh convergence approximate relative error [%]
e_{ext}^{21}	=	mesh convergence extrapolated relative error [%]
$\dot{E}_k$	=	kinetic energy flux rate energy flux rate [W]
$\dot{E}_p$	=	pressure boundary work rate [W]
$\dot{E}_\tau$	=	viscous boundary work rate [W]
$\boldsymbol{f}$	=	volumetric body force vector [N]
$\boldsymbol{F}_{iso}$	=	aerodynamic force vector acting on a body isolated from a propulsor [N]
GCI_{fine}^{21}	=	fine grid convergence index [%]
k	=	thermal conductivity [W/m/K]
L	=	lift force [N]
Ma	=	Mach number [-]
$\hat{n}$	=	surface normal unit vector [-]
N_1, N_2, N_3	=	number of cells in mesh refinements 1,2 and 3 [-]
p	=	static pressure [Pa]
Pr	=	Prandtl number [-]
Q	=	observed order of convergence [-]
r_{21}, r_{32}	=	medium to fine and coarse to medium mesh refinement factors [-]
Re	=	Reynolds number [-]
t	=	time [s]
T	=	static temperature [K]
u, v	=	streamwise and transverse velocity components [m/s]
$\boldsymbol{U}$	=	flight velocity [m/s]

$\mathcal{V}$	=	volume [m^3]
$\boldsymbol{V}$	=	velocity vector in an arbitrary inertial reference frame [m/s]
W	=	weight [-]
$\dot{W}$	=	Work supply rate [W]
$\hat{x}, \hat{y}$	=	unit vectors [-]
$\boldsymbol{X}$	=	position vector [m]
α	=	angle of attack [°]
β	=	lift to drag ratio (L/D) [-]
γ	=	ratio of specific heats [-]
$\dot{\mathcal{E}}$	=	mechanical energy flux rate [W]
Θ	=	volumetric pressure work rate [W]
λ	=	*PER* utilization factor [-]
μ	=	molecular viscosity [kg/m/s]
ν	=	kinematic viscosity [m^2/s]
ρ	=	density [kg/m^3]
τ	=	shear stress [Pa]
$\bar{\bar{\boldsymbol{\tau}}}$	=	viscous stress tensor [Pa]
ϕ_1, ϕ_2, ϕ_3	=	variable for convergence monitoring (C_{DV}) for mesh refinements 1, 2 and 3 [-]
Φ	=	viscous dissipation rate [W]

Subscripts

$(\,)_\infty$	=	freestream quantity, or infinitely large control volume
$(\,)'$	=	energy rate quantity normalized by DV_∞
$(\,)_a$	=	Absolute inertial Reference Frame quantity (ARF)
$(\,)_B$	=	body quantity
$(\,)_e$	=	boundary layer edge quantity
$(\,)_O$	=	control volume outer surface quantity
$(\,)_{\dot{q}}$	=	non-adiabatic quantity

$( )_{\dot{q}=0}$ = adiabatic quantity

$( )_r$ = Relative inertial Reference Frame quantity (RRF)

$( )_{te}$ = trailing edge quantity

$( )_{TP}$ = Trefftz plane quantity

$( )_w$ = wake or wall quantity

I. Introduction

All-electric, hybrid-electric, fuel cells, and alternative fuel combustion systems are currently being developed as part of the civil aviation industries transition away from kerosene fueled propulsion. New approaches to propulsion system integration are being explored to exploit these technologies and simultaneously improve the aerodynamic performance of future aircraft. Boundary Layer Ingestion (BLI) is one such concept which has demonstrated the potential to improve propulsive efficiency, reduce drag and weight [1], firstly by tightly integrating the propulsor into the airframe, but also by partially recovering the energy contained within the boundary layer, mitigating the aircrafts wake and jet losses. Distributed Electric Propulsion (DEP) is an attractive concept due to the inherent flexibility in the quantity, sizing, and positioning of the electric propulsors, which in some configurations takes advantage of BLI as well as offering lift enhancement in wing-integrated designs [2]. The strong aero-propulsive coupling in these configurations means the conventional thrust-drag accounting methods such as those examined by Moirou et al. are not strictly applicable [3]. This has motivated the development of mechanical energy-based [4] and exergy-based [5] analyses, which avoid the ambiguity of assigning thrust and drag contributions all together by directly relating the energy content of the flow to the propulsive power requirement of the vehicle [6].

Whilst there are potentially significant aero-propulsive advantages to these systems, electrifying the propulsion system introduces additional thermal management challenges, due to the acquisition, transportation and rejection of waste heat generated by electric machines, fuel cells and battery systems [7]. Atmospheric heat rejection through surface heat exchangers is a potential solution for electrified aircraft that was examined by Kellerman et al. [8] and Habermann et al. [9], concluding that it may be a viable option for smaller passenger aircraft, or could be used in combination with conventional ram air cooling systems on large aircraft. Early studies have demonstrated that there are circumstantial benefits and penalties of surface heating and cooling on the drag force. In laminar regions of the boundary layer, cooling delays the transition to a turbulent flow thereby reducing skin friction [10], whereas in

turbulent boundary layers, heating reduces skin friction as its influence on shear layers acts as a reduction in the effective Reynolds number [11]. Regardless of the flow regime, laminar or turbulent, heating promotes flow separation [10] [11], whereas cooling has an opposing effect and reduces the pressure drag contributions by decreasing the boundary layer thickness [12]. As a result, some studies show that drag reductions can be achieved by cooling [13] and others by heating [14].

Several more recent studies have applied force-based analyses to 2D Reynolds averaged Navier-Stokes (RANS) computational fluid dynamics (CFD) simulations of airfoils with surface heating and cooling [9] [15] [16]. A limitation of force-based analyses is the recoverable mechanical flow energy cannot be determined, which is relevant to BLI and wake ingesting propulsion systems, as well as formation flight and any configurations with strong propeller wing interactions such as DEP. Conversely, energy or exergy-based approaches provide no means to quantify lift [6]. Therefore, combining both, offers deeper insight by enabling a more extensive flow-field decomposition, as demonstrated by Aguirre and Duplaa [17]. Recovery metrics have been defined under both formulations, the Exergy Waste Coefficient (EWC) [18] and Potential for Energy Recovery (*PER*) by Sanders and Laskaridis [19]. Despite recent developments in energy and exergy-based analyses, and the current thermal management challenge of battery-electric or fuel cell powered propulsion systems, there is a limited number of studies applying these formulations to heated or cooled aerodynamic bodies. Mutangara et al. [20] applied the *PER* metric to the wake energy of various simple adiabatic bodies in isolation, in the works of Arntz and Atinault [21] as well as Lamprakis et al. [22], studies were conducted using simplified fuselage geometry with wall heating, both concluding that there are favorable synergies for waste heat rejection and energy recovery via BLI propulsion systems.

Through an extensive design of experiments (DoE) of 2D RANS CFD cases, this study aims to demonstrate under what circumstances (Re, Ma, α) there are favorable synergies, trade-offs and penalties between surface heating, recoverable energy, and aerodynamic forces. This work is therefore relevant to the development of electrified aircraft with waste heat to reject, and configurations where there is strong airframe-propulsor interaction. A work-energy balance is derived from the generalized governing equations for moving control volumes for a body in dynamic equilibrium in section II. This is combined with the baroclinicity-corrected *PER* metric of Lamprakis et al. [23] in section III to assess the wake energy distribution and recoverable energy of an adiabatic body. Section IV extends this analysis to a non-adiabatic body, to evaluate how thermal gradients influence *PER*, and employs a near-field force equation to simultaneously assess the sensitivity of aerodynamic forces to surface heating and cooling. Finally, the

concept of energy recovery, and the application of the *PER* metric is introduced in the context of wake and boundary layer ingestion using the numerical results and a *PER* utilization factor.

II. Work-Energy Relationships of Flight

A. Inertial Reference Frame Perspectives

In general Newtonian mechanics, Mallinckrodt and Leff [24] describe and emphasize the important distinction between Galilean *invariance* versus Galilean *covariance* in terms of force-momentum versus work-energy relationships, respectively. In other words, force vectors and their momentum counterparts are independent of the inertial reference frame in which they are perceived but work and energy are not. However, Galilean covariance dictates that the change in work perceived through a shift in inertial reference frame will be accompanied by an equivalent change in corresponding energy. This distinction has important implications when considering energy-based approaches to aircraft aerodynamic performance analysis.

Aircraft aerodynamic performance has typically been centered around forces, and, out of convenience, it has become common practice to visualize, calculate, test, and analyze forces with respect to a reference frame fixed to the aircraft. This is referred to herein as the Relative inertial Reference Frame (RRF) in *steady flight*, where the aircraft is perceived to be in *static equilibrium* with the flow moving over it. However, as argued by Renard and Deck [25], Sanders and Laskaridis [19], Sanders [26] [27], and Lamprakis et al. [23], the RRF becomes problematic when attempting to analyze aerodynamics in terms of work-energy relationships, as well as their extensions to exergy analysis [28]. Firstly, static equilibrium is achieved by a forward force (thrust) that directly opposes drag, but in the RRF this thrust force is also perceived to be stationary and therefore doesn't appear to do any work. Secondly, there appears to be an external energy source that continuously supplies the flow-field with streamwise kinetic energy. Therefore, counterintuitively, the atmosphere appears to act simultaneously as both an energy source and sink to the system. Finally, the RRF is only a valid inertial reference frame in *steady flight*, and caution is required when considering other flight regimes to ensure that any work and energy associated with accelerations is properly accounted for.

Instead, to better reflect work-energy relationships it is appropriate to consider an inertial reference frame in which the undisturbed atmosphere is naturally perceived to be in an exergetic dead state, which has also been described by Berhouni et al. [28]. This alternative reference frame intuitively perceives the undisturbed atmosphere to be stationary,

which is without any potential to do work. The aircraft, in this Absolute inertial Reference Frame (ARF)[**], is perceived to move through the initially quiescent atmosphere, imparting energy to the flow that it displaces and disturbs. Unlike the RRF, the ARF is a valid inertial reference frame regardless of the aircraft's flight trajectory, and readily accounts for work-energy transfers of unsteady aircraft motion. Nonetheless, during steady flight, as is the focus of this work, the aircraft is perceived to be in *dynamic equilibrium* from the ARF's point of view instead of *static equilibrium* from the RRF's point of view. In the former, the drag opposing thrust force now acts at the aircraft's flight velocity, thereby doing useful work on the flow via the no-slip condition at the aircraft surfaces. In a simplified explanation, work may be visualized to be initially transferred to the flow in the form of kinetic energy, which then eventually dissipates viscously with time as the aircraft moves on and the atmosphere naturally returns to the exergetic dead once again.

B. Integral Forms of the Fundamental Equations for Moving Control Volumes

To enable the formulation of work-energy relationships of flight in the ARF, Sanders [26] showed that it is necessary to begin with generalized integral forms of the governing equations, that permit the arbitrary motion of a control volume within an arbitrary inertial reference frame. The relations of mass, linear momentum and mechanical energy are given in Eq. (1) to (3), respectively.

$$\frac{\mathrm{D}}{\mathrm{D}t}\iiint_{\mathcal{MV}(t)}\rho\,\mathrm{d}\mathcal{V}=\frac{\mathrm{d}}{\mathrm{d}t}\iiint_{\mathcal{CV}(t)}\rho\,\mathrm{d}\mathcal{V}+\oiint_{\mathcal{CS}(t)}\rho(\boldsymbol{V}-\boldsymbol{V}_{\mathcal{CS}})\cdot\mathrm{d}\boldsymbol{\mathcal{S}}=0 \tag{1}$$

$$\frac{\mathrm{D}}{\mathrm{D}t}\iiint_{\mathcal{MV}(t)}\rho\boldsymbol{V}\,\mathrm{d}\mathcal{V}=\frac{\mathrm{d}}{\mathrm{d}t}\iiint_{\mathcal{CV}(t)}\rho\boldsymbol{V}\,\mathrm{d}\mathcal{V}+\oiint_{\mathcal{CS}(t)}\rho\boldsymbol{V}(\boldsymbol{V}-\boldsymbol{V}_{\mathcal{CS}})\cdot\mathrm{d}\boldsymbol{\mathcal{S}}=\oiint_{\mathcal{CS}(t)}(-p\hat{n}+\bar{\bar{\boldsymbol{\tau}}}\cdot\hat{n})\mathrm{d}\mathcal{S}+\iiint_{\mathcal{CV}(t)}\rho\boldsymbol{f}\,\mathrm{d}\mathcal{V} \tag{2}$$

$$\begin{aligned}\frac{\mathrm{D}}{\mathrm{D}t}\iiint_{\mathcal{MV}(t)}\left(\frac{|\boldsymbol{V}|^2}{2}\rho\right)\mathrm{d}\mathcal{V}&=\frac{\mathrm{d}}{\mathrm{d}t}\iiint_{\mathcal{CV}(t)}\left(\frac{|\boldsymbol{V}|^2}{2}\rho\right)\mathrm{d}\mathcal{V}+\iint_{\mathcal{CS}(t)}\frac{|\boldsymbol{V}|^2}{2}\rho(\boldsymbol{V}-\boldsymbol{V}_{\mathcal{CS}})\cdot\mathrm{d}\boldsymbol{\mathcal{S}}=\\&-\oiint_{\mathcal{CS}(t)}(p\boldsymbol{V}-\bar{\bar{\boldsymbol{\tau}}}\cdot\boldsymbol{V})\cdot\mathrm{d}\boldsymbol{\mathcal{S}}+\iiint_{\mathcal{CV}(t)}(p\nabla\cdot\boldsymbol{V}-\bar{\bar{\boldsymbol{\tau}}}:\nabla\boldsymbol{V}+\rho\boldsymbol{f}\cdot\boldsymbol{V})\mathrm{d}\mathcal{V}\end{aligned} \tag{3}$$

Eq. (1) to (3) relate the time rate-of-change of mass, linear momentum and kinetic energy within an arbitrary material volume in motion, $\mathcal{MV}(t)$, to that experienced by an arbitrary control volume in motion, $\mathcal{CV}(t)$, at the instance in time where the two coincide spatially. The time derivative of an integrated quantity within $\mathcal{CV}(t)$, symbolized by $\frac{\mathrm{d}}{\mathrm{d}t}$,

[**] Following the naming convention of Renard and Deck [25]

does not equate to that of $\mathcal{MV}(t)$, symbolized by $\frac{\mathrm{D}}{\mathrm{D}t}$, due to the relative motion between the two volumes at this instance in time. Following the Leibniz General Transport Theorem, the difference is the net flux in quantity exiting the control volume via its surfaces, $\mathcal{CS}(t)$, which have a different velocity, $\boldsymbol{V}_{\mathcal{CS}}$, relative to that of the fluid, $\boldsymbol{V}$. In Eq. (1) to (3), fluid density, velocity, pressure, and viscous stress tensor are symbolized by ρ, $\boldsymbol{V}$, p, and $\bar{\bar{\boldsymbol{\tau}}}$, respectively. The symbol $\boldsymbol{f}$ accounts for any volumetric body forces acting on the fluid from a distance, which is convenient for including body force representations of propulsion systems. In accordance with convention, the control volume's surfaces are described by a normal vector which points directly out of the volume, such that $\mathrm{d}\boldsymbol{\mathcal{S}} = \hat{n}\mathrm{d}\mathcal{S}$.

The fully generalized forms of Eq. (1) to (3) can be used to describe the flow-field in the ARF [23] [27], represented by a coordinate system $\boldsymbol{X}_a = \langle \hat{x}_a, \hat{y}_a, \hat{z}_a \rangle$. Considering steady flight, the ARF can be related to the RRF, represented by coordinate system $\boldsymbol{X}_r = \langle \hat{x}_r, \hat{y}_r, \hat{z}_r \rangle$, via Galilean transformation, such that:

$$\boldsymbol{V}_a = \boldsymbol{V}_r + \boldsymbol{U} = \boldsymbol{V}_r - \boldsymbol{V}_\infty \tag{4}$$

Where $\boldsymbol{U}$ is the flight velocity (i.e., the reciprocal of the free-stream velocity, $\boldsymbol{V}_\infty$) as well as the velocity at which $\boldsymbol{X}_r$ moves relative to $\boldsymbol{X}_a$. This is useful because it is typically more convenient in CFD to model the aerodynamic body in the RRF and transform the results to the ARF for analysis.

C. Application to Aerodynamic Bodies in Dynamic Equilibrium

When studying the aerodynamics of airframe components, it is convenient to consider them in isolation from the propulsion system. In steady flight, this aerodynamic decoupling makes the implied assumption that dynamic equilibrium is somehow maintained[††]. The effort required must be accounted for by the work-energy balance and may be represented as a supply of work to the body, via an external aerodynamically decoupled force and moment couple, acting directly on the center of mass from a distance to overcome drag, and to counterbalance lift, if not done so by the body's own weight.

Fig. 1 depicts a schematic of an aerodynamically isolated airfoil in steady flight at two instances in time. The external force, $\boldsymbol{F}_{iso}$, acts on the center of mass and at the flight speed to ensure dynamic equilibrium, thereby supplying useful work, $\boldsymbol{F}_{iso} \cdot \boldsymbol{U}$, to the system. This airfoil, along with its encapsulating control volume, is shown to be translating at flight velocity $\boldsymbol{U} = -\boldsymbol{V}_\infty$ with respect to the ARF coordinates, $\boldsymbol{X_a} = \langle \hat{x}_a, \hat{y}_a \rangle$, which are fixed to the

[††] In wind tunnel experiments, balancing forces are provided by the model sting/support, whereas in CFD simulations this balance is enforced via boundary conditions.

page. The RRF coordinates, $\boldsymbol{X}_r = \langle \hat{x}_r, \hat{y}_r \rangle$, and control volume surfaces, are fixed relative to the airfoil and move with the same flight velocity, as perceived by the ARF. For convenience, a rectangular 2D control volume ($\mathcal{CV}$) is assumed, with its control surface ($\mathcal{CS}$) partitioned into an inner surface, $\mathcal{S}_B$, which drapes over the airfoil's surfaces, and an outer surface, $\mathcal{S}_O$, comprised of a front, upper, lower, and rear (Trefftz) plane ($\mathcal{S}_O^{TP}$). The front, upper, and lower outer surfaces are positioned sufficiently far away from the airfoil such that the local fluid is in its exergetic dead state, with $\boldsymbol{V}_a = 0$, $p = p_\infty$ and $T = T_\infty$. In this work, the Trefftz plane is always defined to be perpendicular to $\boldsymbol{U}$ to survey the wake's energy content, and may be located at any position downstream of the airfoil's trailing edge.

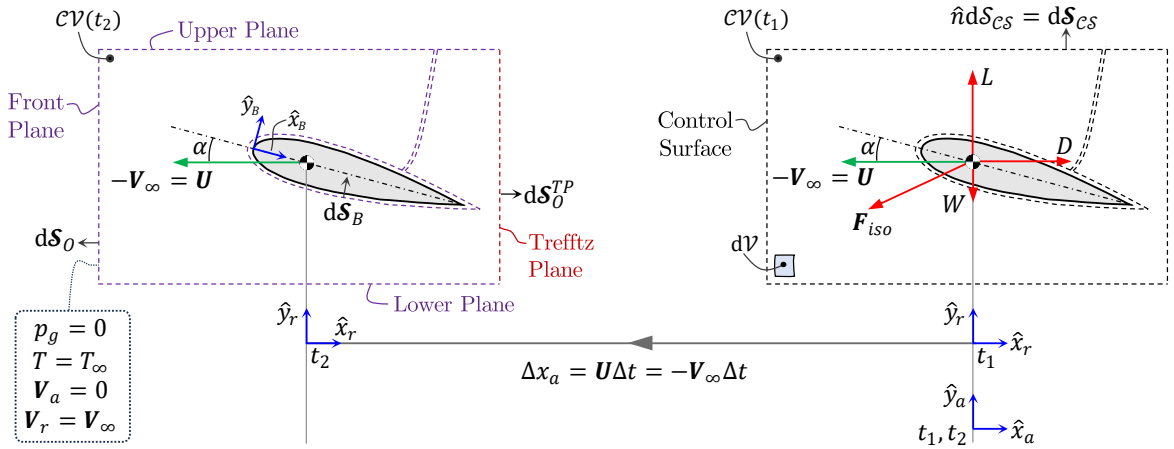

Fig. 1 Moving 2D control volume encapsulating an aerodynamically isolated airfoil in dynamic equilibrium in the ARF, versus the static equilibrium perceived by the RRF.

Applying the ARF momentum-force balance of Eq. (2) to the control volume in Fig. 1, assuming steady flow, and rewriting in terms of gauge static pressure, $p_g = p - p_\infty$, gives the near versus far-field relationship:

$$\iint_{\mathcal{CS}(t)} \left(p_g \hat{n} - \bar{\bar{\boldsymbol{\tau}}} \cdot \hat{n}\right) \mathrm{d}\mathcal{S}_B = -\iint_{\mathcal{CS}(t)} \left(\boldsymbol{V}_a \rho \boldsymbol{V}_r \cdot \hat{n} + p_g \hat{n} - \bar{\bar{\boldsymbol{\tau}}} \cdot \hat{n}\right) \mathrm{d}\mathcal{S}_O \tag{5}$$

The left-hand side of Eq. (5) is the near-field reaction force acting on the airfoil by the fluid and contains the components of both lift and drag. The isolated force that opposes this reaction force, whilst supplying work to the system, is therefore given as:

$$\boldsymbol{F}_{iso} = -\iint_{\mathcal{CS}(t)} \left(p_g \hat{n} - \bar{\bar{\boldsymbol{\tau}}} \cdot \hat{n}\right) \mathrm{d}\mathcal{S}_B = -(D\hat{x} + L\hat{y}) \tag{6}$$

This force acts at a velocity equal to the flight velocity, and the associated work is the dot product between the two:

$$\boldsymbol{F}_{iso}\cdot\boldsymbol{U}=-(D\hat{x}_r+L\hat{y}_r)\cdot(-V_\infty\hat{x}_r+0\hat{y}_r)=DV_\infty=\iint\limits_{\mathcal{CS}(t)}\left(p_g\boldsymbol{V}_\infty-\bar{\bar{\boldsymbol{\tau}}}\cdot\boldsymbol{V}_\infty\right)\cdot\mathrm{d}\boldsymbol{\mathcal{S}}_B \tag{7}$$

The control surface, $\mathcal{S}_B$, moves at the body's flight speed, which is the reciprocal of the free-stream velocity vector, and so the drag power is the work transferred to the flow via the no-slip condition, and can be expressed as:

$$DV_\infty=\boldsymbol{F}_{iso}\cdot\boldsymbol{U}=\iint\limits_{\mathcal{CS}(t)}\left(p_g\boldsymbol{V}_\infty-\bar{\bar{\boldsymbol{\tau}}}\cdot\boldsymbol{V}_\infty\right)\cdot\mathrm{d}\boldsymbol{\mathcal{S}}_B=-\iint\limits_{\mathcal{CS}(t)}\left(p_g\boldsymbol{V}_{\mathcal{CS}}-\bar{\bar{\boldsymbol{\tau}}}\cdot\boldsymbol{V}_{\mathcal{CS}}\right)\cdot\mathrm{d}\boldsymbol{\mathcal{S}}_B \tag{8}$$

Subsequently, this expression of near-field work can be identified within, and made the subject of the work-energy balance, by applying Eq. (3) to the control volume of Fig. 1:

$$\begin{aligned}\underbrace{\iint\limits_{\mathcal{CS}(t)}\left(p_g\boldsymbol{V}_\infty-\bar{\bar{\tau}}\cdot\mathbf{V}_\infty\right)\cdot\mathrm{d}\boldsymbol{\mathcal{S}}_B}_{\boldsymbol{F}_{iso}\cdot\boldsymbol{U}}&=\frac{\mathrm{d}}{\mathrm{d}t}\iiint\limits_{\mathcal{CV}(t)}\left(\frac{|\boldsymbol{V}_a|^2}{2}\rho\right)\mathrm{d}\mathcal{V}+\underbrace{\iint\limits_{\mathcal{CS}(t)}\left(\underbrace{\frac{|\boldsymbol{V}_a|^2}{2}\rho\boldsymbol{V}_r}_{\dot{E}_k}+\underbrace{p_g\boldsymbol{V}_a}_{\dot{E}_p}-\underbrace{\bar{\bar{\boldsymbol{\tau}}}\cdot\boldsymbol{V}_a}_{\dot{E}_\tau}\right)\cdot\mathrm{d}\boldsymbol{\mathcal{S}}_O}_{\dot{\mathcal{E}}}+\underbrace{\iiint\limits_{\mathcal{CV}(t)}-p_g(\nabla\cdot\boldsymbol{V}_a)\,\mathrm{d}\mathcal{V}}_{\dot{\Theta}}\\&+\underbrace{\iiint\limits_{\mathcal{CV}(t)}\bar{\bar{\boldsymbol{\tau}}}:\nabla\boldsymbol{V}_a\,\mathrm{d}\mathcal{V}}_{\dot{\Phi}}\end{aligned} \tag{9}$$

D. Energy Manifestations in the Flow-Field

The first term on the right-hand side of Eq. (9), pertains to the amount of near-field work that manifests as unsteady perturbations of kinetic energy within the flow-field. However, from here, this paper assumes steady level flight, and therefore Eq. (9) reduces to Eq. (10), which with these assumptions is equivalent to the earlier ARF formulated mechanical energy balance of Sanders and Laskaridis [19]. To analyze the power distribution amongst the terms it is useful to normalize Eq. (10) by the drag power ($DV_\infty=\boldsymbol{F}_{iso}\cdot\boldsymbol{U}$), to form Eq. (11), where $(\ )'=\frac{(\ )}{DV_\infty}$.

$$\boldsymbol{F}_{iso}\cdot\boldsymbol{U}=\dot{\mathcal{E}}+\Theta+\Phi \tag{10}$$

$$1=\dot{\mathcal{E}}'+\Theta'+\Phi' \tag{11}$$

Eq. (10) states that the work rate supplied to the body through the action of the isolated force, equals the work input rate to the flow. Via the no-slip condition, this work input manifests as different forms of mechanical energy

throughout the flow-field and can be decomposed into three terms: mechanical energy flux rate ($\dot{\mathcal{E}}$), volumetric pressure work rate (Θ) and a viscous dissipation rate (Φ). The latter two terms are Galilean invariant volumetric quantities which account for physically different loss mechanisms yet are partially coupled through thermo-mechanical interaction. Whereas the first right-hand term constitutes the fluxes of these volumetric quantities, where the flow has not yet returned to the exergetic dead state within the extents of the chosen control volume.

1. Mechanical Energy Flux Rate

Eq. (9) shows that the mechanical energy flux rate ($\dot{\mathcal{E}}$) can be decomposed further into a boundary pressure work rate term ($\dot{E}_p$), kinetic energy flux rate ($\dot{E}_k$), and a viscous boundary work rate ($\dot{E}_\tau$). $\dot{E}_p$ describes the rate at which p_g is doing work on the control surface in the ARF, whereas $\dot{E}_k$ captures the rate that the absolute kinetic energy is crossing the control surface. Following the control volume definition described in section II.C, $\dot{\mathcal{E}}$ need only be calculated over the Trefftz plane as contributions from other surfaces are ≈ 0. A more convenient form is given in Eq. (12), but is only applicable to the control volume described. The viscous boundary work rate ($\dot{E}_\tau$), has been omitted from Eq. (12) because it has been demonstrated, numerically, by Sanders and Laskaridis [19] to have negligible contribution to the work-energy balance.

$$\dot{\mathcal{E}}_{TP} = \iint_{\mathcal{CS}(t)} \left(\underbrace{\rho \frac{(u_a^2 + v_a^2)}{2} u_r}_{\dot{E}_k} + \underbrace{p_g u_a}_{\dot{E}_p} \right) \mathrm{d}\mathcal{S}_O^{TP} \tag{12}$$

2. Viscous Dissipation Rate

In the RRF at the wall $\boldsymbol{V}_r = 0$ due to the no-slip boundary condition, whereas in the ARF $\boldsymbol{V}_a = \boldsymbol{U}$. This viscous interaction between the fluid and the moving wall raises its absolute kinetic energy. At the wall local viscous forces are drawing the fluid along with body, whereas at any distance away from the wall viscous and turbulent shear stresses decelerate the flow dissipating this kinetic energy and irreversibly converting it to internal energy [29]. Therefore, viscosity may be perceived as the enabling mechanism that generates the surplus mechanical energy which forms the boundary layers and the wake. The irreversible nature of viscous dissipation means that Φ is strictly positive. Local viscous losses accumulate throughout the flow field, which intuitively, and mathematically, by Eq. (10), always contribute to an increase in the drag power of the body.

3. Volumetric Pressure Work Rate

Outside of the boundary layers, compressible fluid behavior may be well approximated as a barotropic flow, that is $\rho \approx f(p)$ only, where any significant temperature variation is due to the near isentropic compression and expansion of the fluid. However, in the boundary layers some degree of irreversible self-heating always occurs which leads to a misalignment of the pressure and density gradients, the flow is more precisely described as baroclinic; $\rho = f(p,T)$.

The work of Sato [30] determined that baroclinicity is a requirement for Θ to make a net contribution to the drag power. The dissipative work done by viscous and turbulent shear stresses is accounted for by Φ, but the relatively small amount of expansion work, or positive baroclinic work, due to viscous heating is captured by Θ. Lamprakis [31] identified that baroclinic losses are primarily confined to the boundary layers, meaning that this loss can be well approximated by a volume integral enclosing the body and extending a short distance downstream of the trailing edge where the isentropic energy exchanges have self-cancelled [32]. The total baroclinic loss is therefore the net result of viscous heating and any other heat sources/sinks which do not reach thermal equilibrium isentropically.

E. Wake Energy Decomposition

The simplest application of Eq. (10) is to an inviscid, incompressible flow case. For a 2D airfoil, there are no losses, and the energy balance reduces to $0 = \dot{\mathcal{E}}$ [4], or $-\dot{E}_p = \dot{E}_k$, the pressure and kinetic energy fluxes counterbalance each other exactly. Introducing compressibility yields $-\dot{\mathcal{E}} = \Theta$, which for a flow that has not fully expanded within the extents of its control volume ($\Theta \neq 0$), demonstrates that $\dot{\mathcal{E}}$ contains a counterpart to Θ which accounts for the surface flux rate of the flow's isentropic compression or expansion process. In a viscous flow, the effects of viscosity give rise to surplus mechanical energy, a quantity which is not counterbalanced by the pressure dependent terms, $\dot{E}_p$ or Θ. In the absence of any mechanical energy recovery device, this surplus quantity is ultimately a loss, which is dissipated by turbulent and viscous shear stresses in the boundary layers and the wake, energy which is predominantly accounted for by Φ.

The work-energy balance can be used to provide insight into the wake's energy content and exchange pathways. Fig. 2 illustrates the general energy trends for an isolated body in steady level flight, moving through a compressible viscous fluid. Fig. 2 depicts that at an infinite distance downstream[‡‡] the energy distribution consists of only global losses, $\Theta_\infty + \Phi_\infty$. In terms of drag power fractions, Φ' has accumulated and asymptotes towards a value equal to $(1 -$

[‡‡] Where $\boldsymbol{V}_a = 0$ and $p_g = 0$.

Θ'_∞). Taking the spatial derivative of Eq. (10) in the freestream direction ($\hat{x}$) yields Eq. (13) and shows that the rate Φ accumulates is equal to the decay rate $\dot{\mathcal{E}} + \Theta$.

$$\frac{\mathrm{d}\Phi}{\mathrm{d}x} = -\left(\frac{\mathrm{d}\dot{\mathcal{E}}}{\mathrm{d}x} + \frac{\mathrm{d}\Theta}{\mathrm{d}x}\right) = -\left(\frac{\mathrm{d}\dot{E}_k}{\mathrm{d}x} + \frac{\mathrm{d}\dot{E}_p}{\mathrm{d}x} + \frac{\mathrm{d}\Theta}{\mathrm{d}x}\right) \tag{13}$$

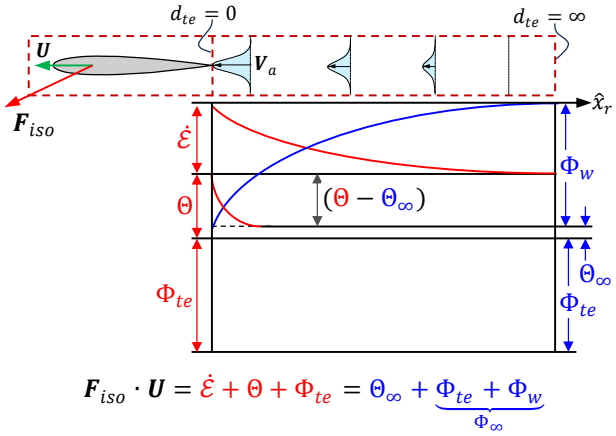

Fig. 2 General application of Eq. (10) to an array of control volumes with the Trefftz plane progressively moving downstream from the trailing edge to infinite.

A consequence of Φ being strictly positive is that $\mathrm{d}\Phi/\mathrm{d}x$ must also be positive. For an incompressible flow Eq. (13) reduces to $\frac{\mathrm{d}\Phi}{\mathrm{d}x} = -\frac{\mathrm{d}\dot{\mathcal{E}}}{\mathrm{d}x}$, there is a direct exchange of energy between the two terms. Close to the trailing edge and outside of the boundary layers, a significant portion of the energy is due to the relatively inviscid exchange between the pressure and velocity fields. Downstream of the body, the pressure field recovers over a short distance and as a result $\frac{\mathrm{d}\dot{E}_p}{\mathrm{d}x} \approx 0$ (see Fig. 5). The accumulation of Φ' reaches a maximum as the wake's kinetic energy asymptotes to zero, $\frac{\mathrm{d}\Phi}{\mathrm{d}x} \approx -\frac{\mathrm{d}\dot{E}_k}{\mathrm{d}x}$. Similarly, in compressible flows, there is a rapid decay of Θ a short distance downstream of the trailing edge and the dissipative exchange of Φ and $\dot{E}_k$ persists into the far-field.

F. Potential for Energy Recovery

The Potential for Energy Recovery (*PER*) metric first introduced by Sanders and Laskaridis [19] represents the fraction of the total drag power that has not yet been converted irreversibly to internal energy. Lamprakis et al. [23] further developed the metric to incorporate the baroclinic loss realized by Sato [30]. As *PER* constitutes the flow's recoverable mechanical energy, it can, theoretically, be completely and directly converted to useful work by an ideal

mechanical energy device [33], as opposed to the conversion of heat to useful work, which is limited by the Carnot efficiency. *PER* may be applied to quantify the portion of the wakes energy at a given Trefftz plane position that could hypothetically be recovered by a BLI or wake ingesting propulsor.

For incompressible flows, absent of baroclinic losses, the original formulation [19] is applicable:

$$(PER)_{TP} = 1 - \Phi'_{TP} \tag{14}$$

For compressible flows, the baroclinicity corrected form [23] should be applied. This utilizes the calculation of the global baroclinic work, Θ_∞, which, strictly speaking, makes Eq. (15) an approximation as there will be local baroclinic losses that exist within the chosen control volume. The assumption that these local losses are approximately equal to the global loss is valid as the baroclinic losses are predominantly confined to the boundary layers [31].

$$(PER)_{TP} \approx 1 - (\Theta'_\infty + \Phi'_{TP}) \tag{15}$$

In practice, the calculation of Θ_∞ is performed by computing the integral over the entire CFD domain.

III. Energy Analysis of an Airfoil with Adiabatic Walls

Steady 2D RANS CFD simulations have been performed on the NACA0012 airfoil with an adiabatic wall boundary condition. Eq. (10) is applied to decompose the wake energy content, enabling *PER* to be calculated via Eq. (15). A rectangular control volume is assumed, following the description in section II.C. The front and side planes are fixed with respect to the CFD domain and positioned sufficiently far away such that their contributions to $\dot{\mathcal{E}}$ are ≈ 0. Further details of the computational model, as well as a domain size and grid refinement study can be found in the appendix. The freestream temperature (T_∞) was held constant with the foresight of any future experimental work, which would require control of the two predominantly temperature dependent non-dimensional parameters Pr_∞ and γ_∞. The angle of attack (α), as well as the Reynolds and Mach number have been varied independently of one another whilst holding the others constant. The conditions simulated are listed in Table 1 and are limited to subsonic freestream flows, α that avoid the stall region to ensure steady flow, and turbulent Reynolds numbers, based on the turbulent flow threshold for smooth flat plates [34].

Table 1 Adiabatic design of experiments

Property	Range
Re_∞	10^6, 10^7, 10^8
Ma_∞	0.15, 0.30, 0.45, 0.60
α	0, 2, 4, 6, 8°

The *PER* metric is applicable to any control volume with its Trefftz plane located at or downstream of the trailing edge. Fig. 3 demonstrates the downstream decay of *PER* for a symmetric flow, due to the accumulation of Φ. For the flow cases studied, different Mach number curves coincide with one another, as initially observed by Lamprakis et al. [23]. A deviation exists close to the trailing edge, but as shown by Fig. 4, *PER* becomes independent of the Mach number within ½ a chord. Therefore, total energy losses for a symmetric flow with adiabatic walls depend solely on the Reynolds number, higher *Re* increasing the viscous dissipation rate, thereby reducing *PER*.

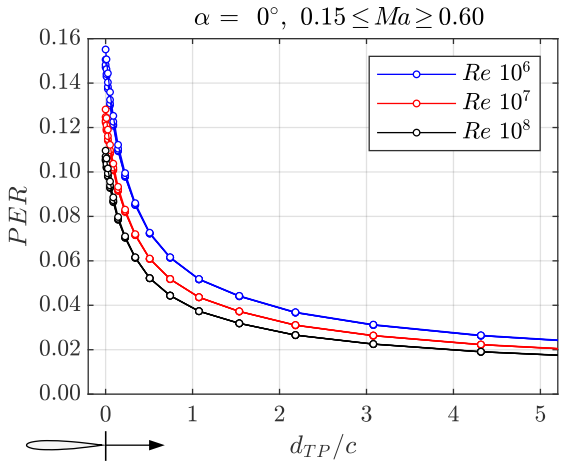

Fig. 3 Decay of *PER* downstream of the trailing edge for $0.15 \leq Ma \geq 0.60$, fixed *Re* and $\alpha = 0°$.

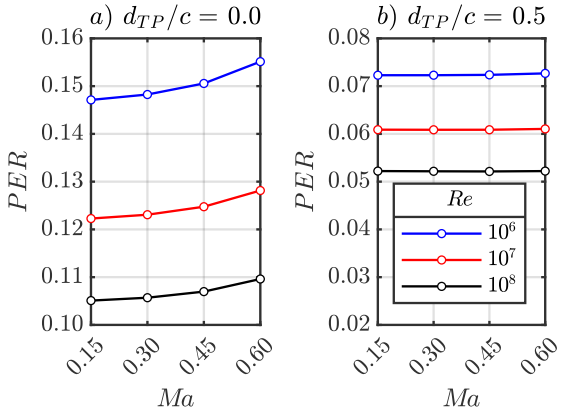

Fig. 4 *PER* versus *Ma* for a non-lifting flow, a) Compressibility dependent *PER* at trailing edge, b) Compressibility independent *PER* ½ chord downstream.

The wake energy distribution is however influenced by the Mach number. Fig. 5 shows that close to the trailing edge there is a rapid exchange between the energy constituents. Increasing Mach number amplifies this behavior, due to the strong response of the pressure field to fluid compressibility. These pressure gradients are predominantly a response to the curvature and stagnation of the flow, which there is little of in the wake, and at $d_{TP}/c > 2$ the energy distribution again depends only on *Re*, as $\dot{E}_k$ gradually decays and Φ asymptotes towards the global value shown in Fig. 6. The combination of high freestream *Ma* and *Re* can yield the unique result of negative $\dot{\mathcal{E}}$. The increased dissipation rate reduces $\dot{E}_k$ and therefore $|\dot{E}_p| > |\dot{E}_k|$. This is accompanied by positive $\frac{\mathrm{d}\mathcal{E}}{\mathrm{d}x}$ close to the trailing edge, by Eq. (13) as Φ is strictly positive $\dot{\mathcal{E}}$ must return to a positive value as $\frac{\mathrm{d}\Theta}{\mathrm{d}x}$ approaches zero. It is important to note, that negative $\dot{\mathcal{E}}$ should not be interpreted as a source of thrust or energy, but rather, a result of the decomposition, as for flow conditions that produce it, it is compensated for by increased dissipation and locally counterbalanced by Θ.

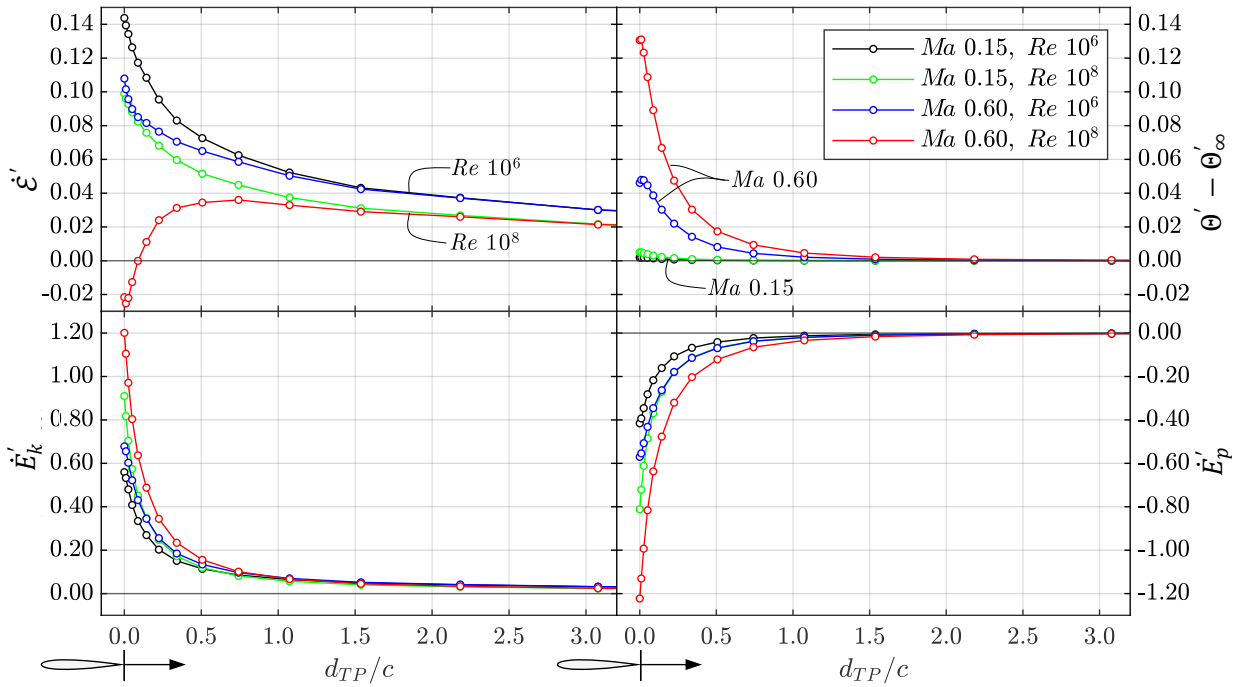

Fig. 5 Incompressible and compressible flows for $\alpha = 0^{\circ}$. Top left: $\dot{\mathcal{E}}'$, top right: $(\Theta' - \Theta'_{\infty})$ decay of volumetric pressure work, bottom left: $\dot{E}'_k$, bottom right: $\dot{E}'_p$.

As the freestream Mach number increases, density gradients in the flow become stronger. Subsequently, localized compression and expansion of the viscous fluid contributes to a net increase in internal energy. A small amount of work done is done by the local flow expanding against its surroundings caused by viscous heating, contributing to

Θ_∞. Whilst *PER* has been shown (Fig. 3) to be circumstantially independent of *Ma*, Fig. 6 shows how *Ma* influences the global energy distribution, increasing baroclinic losses (Θ'_∞) and reducing the viscous dissipation (Φ'_∞). For the adiabatic airfoil cases shown, the Θ'_∞ residual accounts for a relatively insignificant portion of the total power distribution but does become significant for flows with heat sources/sinks and is discussed further in section IV.

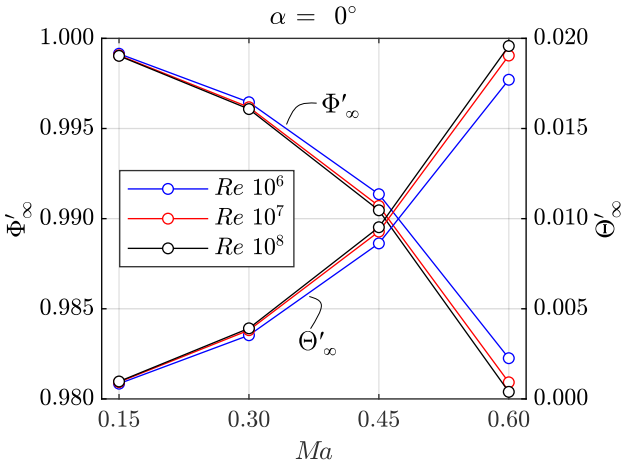

Fig. 6 Influence of *Ma* on both viscous and compressibility associated losses.

Fig. 7 shows that within the limits of stall, *PER* increases with angle of attack. Neglecting the small contribution from Θ'_∞, the increase can be attributed to a reduction in Φ in the boundary layers.

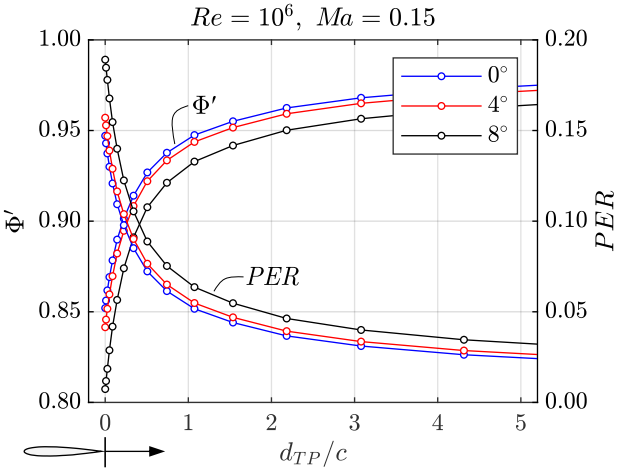

Fig. 7 Progression of *PER* and the viscous dissipation fraction in the wake for α = 0°, 4°, 8°.

To examine this further, a C_p distribution is shown in Fig. 8. For increased α there is a clear reduction in pressure on the upper surface associated with lift, this is accompanied by a region of adverse pressure. At the wall in the RRF, the

momentum equation reduces to the viscous and pressure terms only, Eq. (16), revealing that in adverse pressure the flow curvature at the wall must be positive.

$$\frac{\partial p}{\partial s} = \frac{\partial \tau}{\partial n} = \mu \frac{\partial^2 u}{\partial n^2}\bigg|_w \tag{16}$$

This naturally reduces the wall velocity gradient $\frac{\partial u}{\partial n}\big|_w$, reducing shear stress and viscous dissipation Φ, in the ARF more kinetic energy has been imparted to the flow. As global losses are governed by *Re*, the inevitable viscous dissipation is shifted downstream to the wake. On the lower surface an opposing effect can be observed from Fig. 8, a region of favorable pressure exists beyond the stagnation point (x_B/c where $C_p = 1$). However, the subtle shift in stagnation point and the prolonged region of favorable pressure, alters the distances at which these two opposing effects take place, producing the net result of increased *PER*.

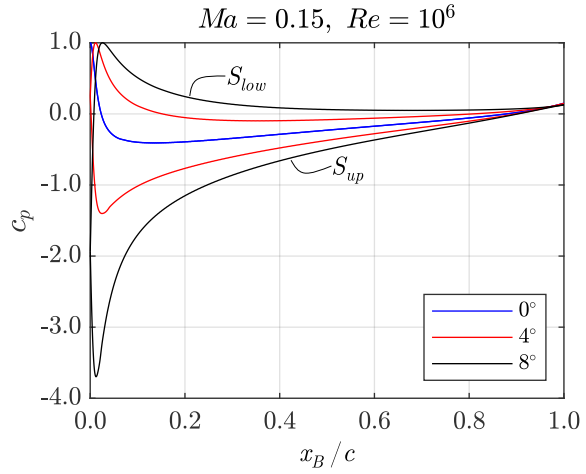

Fig. 8 C_p distribution comparison for α = 0°, 4°, 8°, *Ma* = 0.15, *Re* = 10^6

IV. Force and Energy Analysis of an Airfoil with Non-Adiabatic Walls

Introducing a heat source or sink at the wall causes a local change in fluid properties that can have a significant effect on the boundary layer, the resulting energy balance, and the aerodynamic force vector, prompting analyses in both the force and energy domain. The energy analyses consider only the streamwise force component aligned with ***U*** [6], as the lift force is typically defined to be perpendicular to the direction of motion [35] it does no work, and therefore makes no direct contribution to the energy exchange between the body and its surroundings. However, the aspects of the flow field that facilitate lift do influence the streamwise force and the wake energy distribution.

To explore the influence of wall heating and cooling on the flow physics in both the force and energy domains, a second DoE has been performed over a wide range of uniform wall temperatures, whilst maintaining the 300K freestream temperature. Wall (T_w) to freestream (T_∞) temperature ratios listed in Table 2 have been simulated for a range of *Re*, *Ma* and α, within the same limits of turbulent, steady, and subsonic flow from section III.

Table 2 Non-adiabatic design of experiments

Property	Range
Re_∞	10^6, 10^7, 10^8
Ma_∞	0.15, 0.60
α	0, 2, 4°
T_w/T_∞	6/9, 7/9, 8/9, 1.0, 1.5, 2.0, 2.5, 3.0

A. Effect of Surface Heat Transfer on the Boundary Layer

Heating decreases the density of air and increases its molecular viscosity, the ratio of the two increases momentum diffusivity, $\nu = \mu/\rho$. In the absence of additional forces, the reduction in density naturally increases the thickness of the boundary layer. Heating the wall generates both a negative temperature and viscosity gradient in the wall normal direction, and an additional term arises in Eq. (16) when $\frac{\partial \tau}{\partial n}$ is expanded out, to give Eq. (17). White [34] summarizes the work of Reshotko [10], which, using Eq. (17), describes how the wall temperature affects the near-wall curvature. Due to the negative viscosity gradient, in adverse pressure gradients wall heating can only increase the near-wall curvature, pushing the flow closer to separation.

$$\mu \frac{\partial^2 u}{\partial n^2}\bigg|_w = \frac{\partial p}{\partial s} - \frac{\partial u}{\partial n}\frac{\mathrm{d}\mu}{\mathrm{d}n} \tag{17}$$

Fig. 9 demonstrates this local behavior at x_B/c = 0.9, where there is more positive $\frac{\partial^2 u}{\partial n^2}\Big|_w$, reduced $\frac{\partial u}{\partial n}\Big|_w$ and increased boundary layer thickness (n_e) for greater wall temperatures.

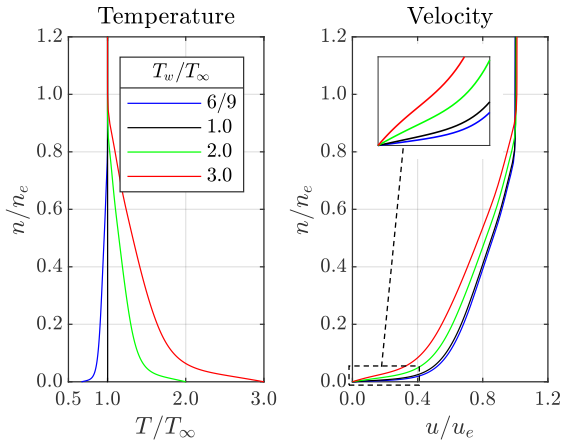

Fig. 9 Boundary layer velocity and temperature profiles normalized by T_∞, u_e and n_e for a range of T_w, at x_B/c = 0.9 for Ma = 0.15, Re = 10^6 and $\alpha = 0^\circ$.

There are, however, more subtle factors that contribute to these changes in the boundary layer. Heating the laminar portion of the boundary layer has been shown to destabilize the flow [34], early workers discussed the use of wall cooling to delay the onset of turbulence [10]. Therefore, the thicker boundary layer for higher wall temperatures is partly due to a shift of the transition point towards the leading edge. At the same x_B/c the turbulent boundary layer of a heated wall is more developed and thus thicker. Furthermore, the pressure and density gradients now have components that lie perpendicular to one another and the baroclinic torque term ($\frac{1}{\rho^3}\nabla\rho \times \nabla p$) in the vorticity transport equation is non-zero [36]. In adverse pressure gradients, the low-density fluid parcels close to the wall are decelerated more-so than those further away[§§], pushing the velocity profile towards the less stable condition of positive near-wall curvature $\frac{\partial^2 u}{\partial n^2}$ as can be seen in Fig. 9 for $\frac{T_w}{T_\infty} = 2 \rightarrow 3$.

B. Near-Field Force Decomposition

1. Drag Force

The change in the viscous and pressure drag components relative to the adiabatic case for different ratios of T_w/T_∞ is shown in Fig. 10 for all the flow cases simulated. Two general trends can be clearly seen; heating reduces the viscous drag and increases the pressure drag, as may be deduced from Refs. [11] [12]. The opposite is observed for wall cooling. The reduction in $\frac{\partial u}{\partial n}\Big|_w$ with heating, that was discussed in the previous section, combined with the small

[§§] Assuming only minor variation in $\partial p/\partial s$ in the wall normal direction

increase in molecular viscosity, evidently, produces a net reduction in wall shear stress, $\tau_w = \mu \frac{\partial u}{\partial n}\Big|_w$, which is consistent with the work of Mabey [11].

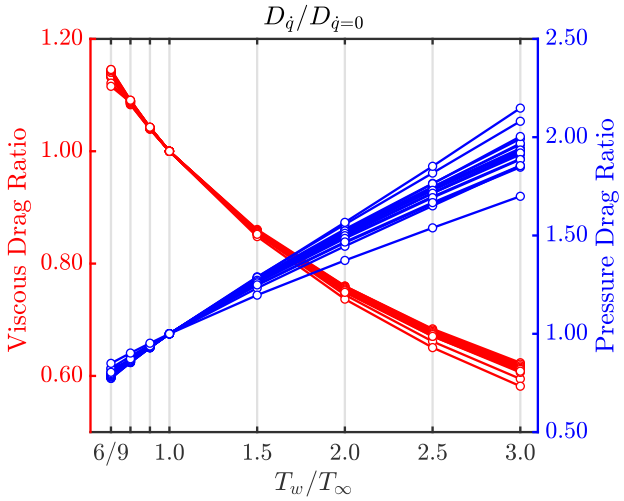

Fig. 10 Change in viscous and pressure drag components for all non-adiabatic flow cases simulated, normalized by the drag component of the adiabatic case.

The increase in the pressure drag results from the difference between the surface pressure distribution on the fore and aft parts of the body. Fig. 11 compares the C_p distribution for different T_w/T_∞ for a non-lifting flow of low *Ma* and *Re*. It shows that the difference in the pressure field is only significant towards the trailing edge, the stagnation pressure at the leading edge is virtually unchanged by the presence of a temperature gradient. The delayed recovery of the pressure field and the resulting increase in pressure drag in heated flows must therefore be due to the reduction in the pressure gradient tangent to wall, on average over the length of the body. At the wall where the pressure and viscous shear forces are in equilibrium, the reduction in the viscous force has a direct influence on pressure distribution by reducing the strength of the pressure gradient, delaying the recovery of the pressure field, and increasing the pressure drag. Similarly, the pressure drag increases by reducing Re_∞ for both the adiabatic and non-adiabatic case.

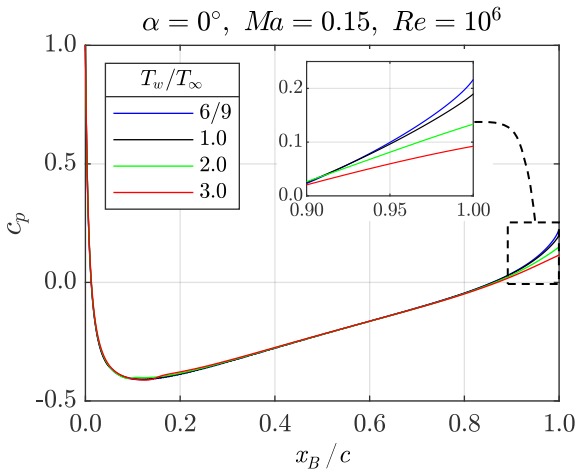

Fig. 11 C_p distribution comparison for a range of T_w/T_∞ for $\alpha = 0^\circ$, $Ma = 0.15$, $Re = 10^6$

The change in the total drag (D_T) depends on the significance of the pressure drag component of the adiabatic case. Fig. 12 highlights the two extremes, where heating has produced opposing trends. Low *Ma*, high *Re* and $\alpha = 0^\circ$ is a viscous dominant flow case, characteristic of thin boundary layers. Heating therefore reduces the total drag across the temperature range studied, whereas the pressure drag for a high *Ma*, low *Re* and $\alpha > 0^\circ$ is already significant, and heating of the walls amplifies this effect, increasing in the total drag.

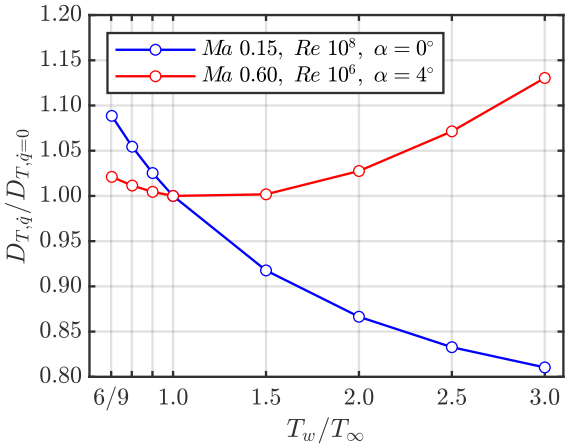

Fig. 12 Total drag force comparison between conditions which maximize the pressure drag and minimize the viscous drag.

2. Lift Force

The generation of lift ultimately requires flow asymmetry across the upper and lower surfaces. Asymmetry is typically achieved through combination of angle of attack and cambered geometry. Much less practically, non-uniform heating or cooling of the surfaces can also meet the flow asymmetry requirement. Samiee et al. [15] showed that

heating the lower surface only generates lift[***] for symmetric geometry with $\alpha = 0^{\circ}$, heating of the upper surface would therefore produce a downforce. This agrees with Kallath et al. [16] work on local heating, for $\alpha > 0^{\circ}$ they conclude that heating the lower surface close to the trailing edge can augment the lift force, whilst heating the upper reduces it. Uniform heating therefore combines the effects of the upper surface lift reduction and the lower surface lift increase, Fig. 13 shows the net result for $\alpha > 0^{\circ}$. The lift force is reduced linearly, behavior that is consistent across all flow cases and most sensitive to the same conditions which have a significant pressure drag component (low *Re*, high *Ma*). This net result demonstrates that for the same wall temperature the upper surface exhibits a greater sensitivity to heat rejection than the lower. This is due to the upper surface boundary layer predominantly being a region of adverse pressure for $\alpha > 0^{\circ}$ (Fig. 8), and the effect that this has combined with the temperature gradient on the near wall curvature as discussed in section IV.A.

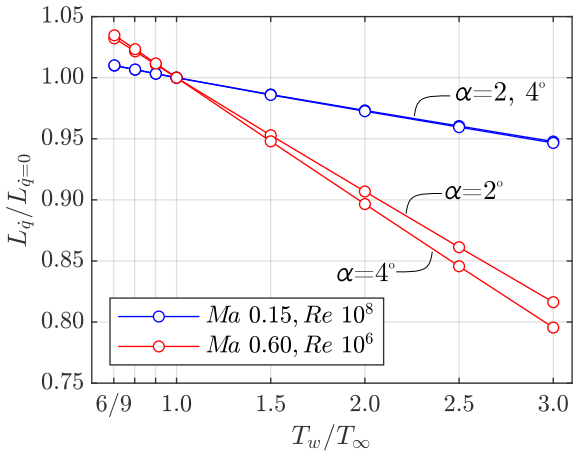

Fig. 13 Change in lift force against T_w/T_∞.

Fig. 14 shows the surface pressure distribution for different T_w/T_∞ at $\alpha = 4^{\circ}$. The forebody makes the largest local contribution to the lift force[†††] and is also the region where the most noticeable change occurs across different T_w. The magnitude of the stagnation pressure is unchanged by heating; however, the tangential pressure gradient along the upper surface is less favorable in the vicinity of the stagnation point, reducing the drop in pressure. McLean [37] discusses the reciprocal nature of the forces exerted on a fluid parcel and the inertia that sustains them. In the case of a heated wall, the reduction in density acts to reduce the magnitude of the fluid parcels inertia, and the strength of the pressure force ($\partial p/\partial s$) reduces accordingly.

[***] Or cooling of the upper surface only
[†††] The region with the largest Δp across the upper and lower at the same x_B/c position

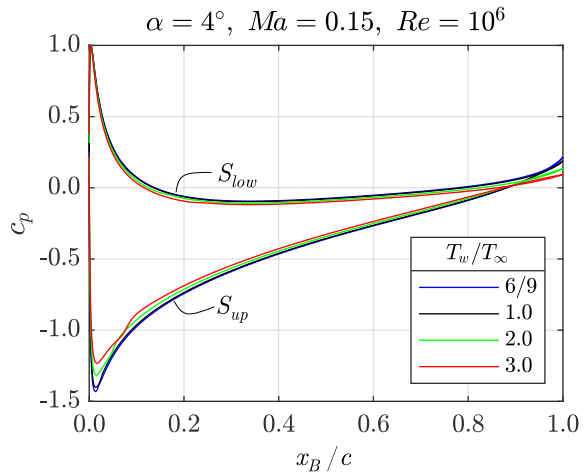

Fig. 14 Wall pressure distribution comparison for a range of T_w/T_∞, $\alpha = 4^\circ$, $Ma = 0.15$, $Re = 10^6$.

The discussion up to this point has focused on the surface pressure and the implications for the near field integral, the far-field integral provides an alternative perspective of the same phenomena. The equation may be formed by substituting the far-field relationship of Eq. (5) into Eq. (6) and taking the dot product with $\hat{y}$ from Fig. 1:

$$L = -\boldsymbol{F}_{iso} \cdot \hat{y} = \left(- \iint_{\mathcal{CS}(t)} \left(\boldsymbol{V}_a \rho \boldsymbol{V}_r \cdot \hat{n} + p_g \hat{n} \right) \mathrm{d}\mathcal{S}_O \right) \cdot \hat{y} \tag{18}$$

Assuming a control volume of infinite depth with a finite distance between its parallel front and Trefftz planes eliminates the pressure contributions [38] [39] from Eq. (18). This leads to Eq. (19) and the lift force may now be observed as the change in transverse momentum (ρv_a) between the two planes:

$$L = \int_{-\infty}^{+\infty} (\rho v_a) u_r \, \mathrm{d}\mathcal{S}_O^{FP} - \int_{-\infty}^{+\infty} (\rho v_a) u_r \, \mathrm{d}\mathcal{S}_O^{TP} \tag{19}$$

Local heating increases the fluids momentum diffusivity ($\nu = \mu/\rho$), reducing the rate that transverse momentum (ρv_a) is imparted to the wake, leading to a reduction in lift. As demonstrated by Fig. 13, cooling has the opposite effect, the increase in density and fluid inertia produces a strong downward deflection of the flow at the trailing edge increasing the lift force.

3. Aerodynamic Efficiency

The effect of uniform surface heating and cooling has been assessed for both lift and drag independently of one another, demonstrating that cooling can increase the lift force whilst heating decreases it. The drag force does not exhibit the same monotonic behavior, as for the same T_w/T_∞, there may be a penalty or a benefit depending on the

flow case. To understand the implications for the overall aerodynamic performance, the L/D ratio (β) must be assessed as the two force components are intrinsically coupled. Fig. 15 shows this relationship between β and T_w/T_∞, for a combination of *Ma* and *Re* that showcase the full range of β sensitivity to wall temperature.

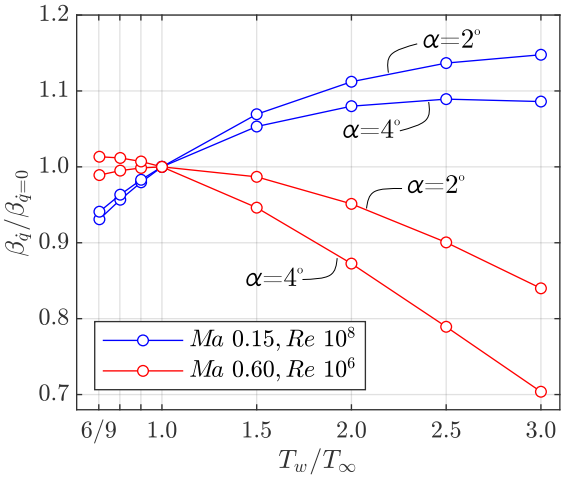

Fig. 15 Lift to drag ratio of the non-adiabatic case normalized by the adiabatic case against T_w/T_∞.

Assuming the lift requirement is unchanged, the reduction by uniform heating would require an increase of α, further increasing the drag towards a more pressure dominant case and potentially eliminating any aerodynamic benefit of surface heating. Fig. 15 shows that surface heating may improve the aerodynamic efficiency of a viscous dominant combination of low *Ma* and high *Re* due to the total drag reduction from Fig. 12 outweighing the reduction in lift. High *Ma* and low *Re* cases, as shown, are subject to both a severe lift and drag penalty. A small benefit at $\alpha = 4°$ may be observed for surface cooling, which is the net result of increased lift and a reduction in pressure drag.

C. Mechanical Energy Decomposition

The trends of total drag force ratio ($D_{\dot{q}}/D_{\dot{q}=0}$) shown in Fig. 12 are identical to a drag power ratio, with negligible numerical difference between the two calculation methods, as demonstrated by the grid and domain size studies in the appendix. The work-energy balance provides additional insight into the losses, with a more extensive decomposition, not limited to just the viscous and pressure drag contributions. A consequence of wall heating is the portion of viscous dissipation that occurs over the body is reduced, and the loss is shifted downstream to increase the wake portion, as shown by Fig. 16. The wake region is defined from the trailing edge of the airfoil to an infinite distance downstream[‡‡‡]

[‡‡‡] For the numerical calculation the extent of the CFD domain is used.

and is calculated by Eq. (20), where Φ_{te} is calculated over a control volume with its Trefftz plane located at the trailing edge ($d_{TP}/c = 0$), and the surface normal parallel to the freestream velocity vector:

$$\Phi_w = \Phi_\infty - \Phi_{te} \tag{20}$$

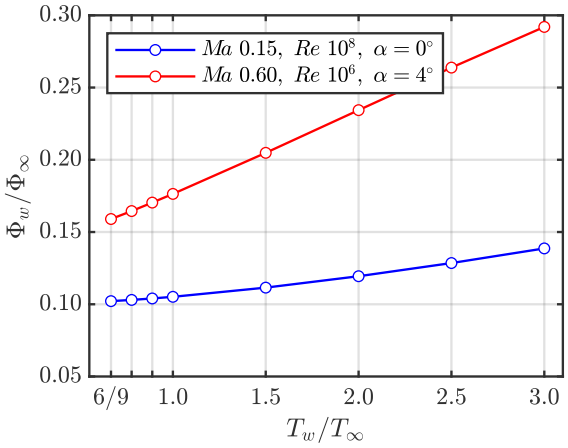

Fig. 16 Viscous dissipation of the wake region normalized by the total viscous dissipation against T_w/T_∞.

The reduced boundary layer dissipation leaves a larger portion of $\dot{\mathcal{E}}$ and $(\Theta - \Theta_\infty)$ remaining at the trailing edge, increasing *PER* at this location as shown by Fig. 17.

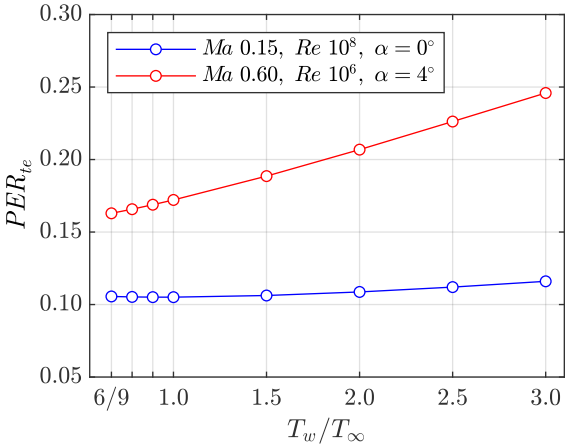

Fig. 17 *PER* at the trailing edge against T_w/T_∞.

The downstream decay of *PER* is presented in Fig. 18. Away from the trailing edge, *PER* is largely unaffected by the upstream heat rejection over the wide range of T_w/T_∞ that were simulated. Therefore, as was shown for an adiabatic airfoil, wake dissipation is governed predominantly by Re_∞ as $\frac{d\Phi}{dx}$ is practically independent of T_w/T_∞ beyond a Trefftz plane distance of ½ a chord (Fig. 18.b).

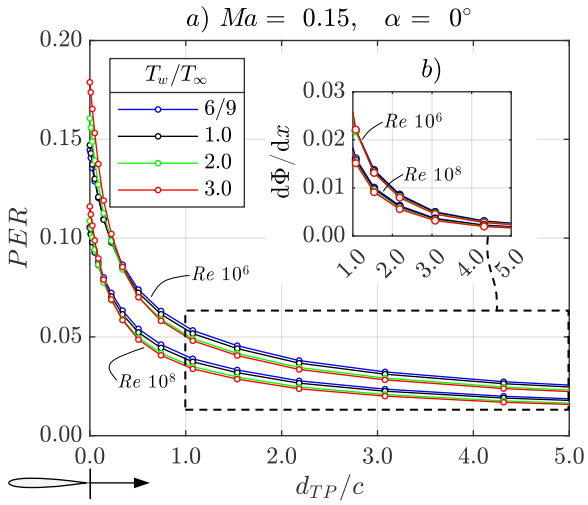

Fig. 18 a) Downstream decay of *PER*, *Ma* = 0.15, $\alpha = 0^\circ$, b) Viscous dissipation gradient against Trefftz plane position.

Within ½ a chord downstream, the trend shown in Fig. 17 is reversed and persists into the far-field. *PER* now reduces with increasing T_w due to the increase in Φ'_w and Θ'_∞. Naturally there is a crossover point, which occurs marginally earlier for greater *Re*, due to the higher baroclinic work that is shown in Fig. 19. The portions of viscous and compressibility associated loss have changed significantly from that of the adiabatic case (Fig. 6).

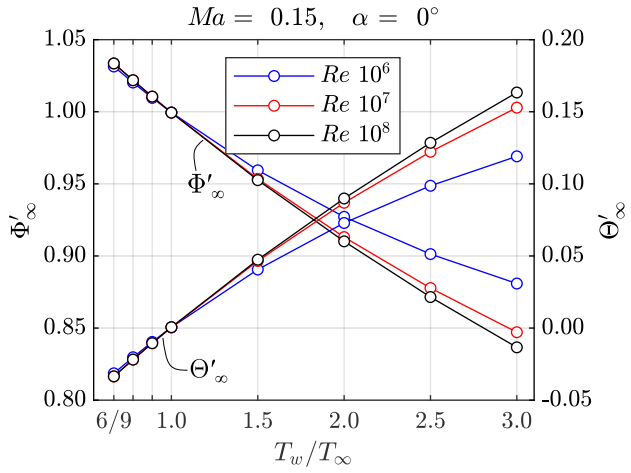

Fig. 19 Wall heating influence on the viscous and compressibility associated losses at an infinite distance downstream of the trailing edge for a non-lifting 'incompressible' Mach number.

In the case of heating, work must be done by the local flow to displace the surroundings for the density gradients to exist. Simultaneously, the reduction in fluid density lessens the strength of the velocity gradients and therefore reduces the magnitude of the viscous shear stresses and Φ'. With a sufficiently large heat sink, Θ'_∞ becomes negative, and is accompanied by $\Phi'_\infty > 1$, such that the work-energy balance is maintained. The same mechanism which

increases Θ'_∞ for heating, reduces Φ'. Fig. 19 demonstrates that when heat sources or sinks are present, compressibility associated (Θ'_∞) losses can become significant even for 'incompressible' Mach numbers. Sanders and Laskaridis [19] note that some previous studies employing energy-based analyses, account for Θ's contribution to the drag power by applying an assumed correction to Φ. This appears to be an unnecessary approximation and its implications could be particularly important for the accurate modelling of aero-propulsive configurations or surface heat exchangers.

D. Considerations for Energy Recovery

Establishing a well-defined measure of how much energy is theoretically recoverable is a logical first step prior to the development of an energy recovering device. In previous sections, the rationale behind computing *PER* for the body in isolation was to clearly distinguish between conditions which minimize and maximize the recovery potential. An energy recovering device aims to utilize the available *PER* at its inlet, to reduce the work supply rate from the aircrafts on board energy ($\dot{W}$), such that $\frac{\dot{W}}{DV_\infty} < 1$. This concept may be expressed as Eq. (21), where a non-dimensional *PER* utilization factor is introduced, λ, which may be ≤ 1. $\lambda = 1$ represents the ideal scenario where all *PER* is utilized, in the event of adverse propulsor-body interaction effects $\lambda < 0$ and therefore $\frac{\dot{W}}{DV_\infty} > 1$.

$$\frac{\dot{W}}{DV_\infty} = 1 - \lambda(PER) \tag{21}$$

For real aircraft and propulsor geometry, demonstrating the aero-propulsive benefit of an energy recovering configuration requires comparison against a chosen baseline. The choice of baseline is somewhat arbitrary, as discussed by Hall et al. [40], however, in this section, where the airfoil body remains unchanged and the propulsor is conceptual, it is justifiably selected to be the adiabatic body in isolation. Eq. (21) is rearranged to make $\dot{W}$ the subject and then normalized by $(DV_\infty)^{iso}_{\dot{q}=0}$ to form Eq. (22), which is applied in Fig. 20. The aim here is to qualitatively show the potential reduction in $\dot{W}$ under different flow and heating conditions for $0 \leq \lambda \leq 1$. Here it is assumed that propulsor-body interaction effects are negligible, such that $(DV_\infty)^{iso}_{\dot{q}} = (DV_\infty)^{rec}_{\dot{q}}$ and $(PER)^{iso} = (PER)^{rec}$.

$$\frac{\dot{W}^{rec}_{\dot{q}}}{\dot{W}^{iso}_{\dot{q}=0}} = \frac{(DV_\infty)_{\dot{q}}}{(DV_\infty)^{iso}_{\dot{q}=0}}[1 - \lambda(PER)] \tag{22}$$

These assumptions are valid for wake ingestion[§§§] [40] [41], and have been shown to be a reasonable approximation for simplified BLI configurations[****] on axisymmetric fuselages and flat plates [40] [41]. The approximation, $(DV_\infty)^{iso} \approx (DV_\infty)^{bli}$, holds for turbulent Re_∞ [23], but may be less accurate for a powered airfoil or wing, as interaction effects are enhanced by greater ratios of propulsor diameter to body chord length [30]. Fig. 20 compiles the results of the non-adiabatic DoE for $\alpha = 0^\circ$ and $\alpha = 4^\circ$, to show the relation between freestream conditions (Re_∞, Ma_∞), wall temperature, $(PER)_{te}$ and the non-adiabatic to adiabatic drag power ratio $(DV_\infty)_{\dot{q}}/(DV_\infty)_{\dot{q}=0}$. The drag power ratio map (shaded green) shows where there are purely aerodynamic benefits and penalties of heating and cooling relative to the adiabatic case, whereas including $(PER)_{te}$ shows where there are potential aero-propulsive opportunities for an energy recovering device.

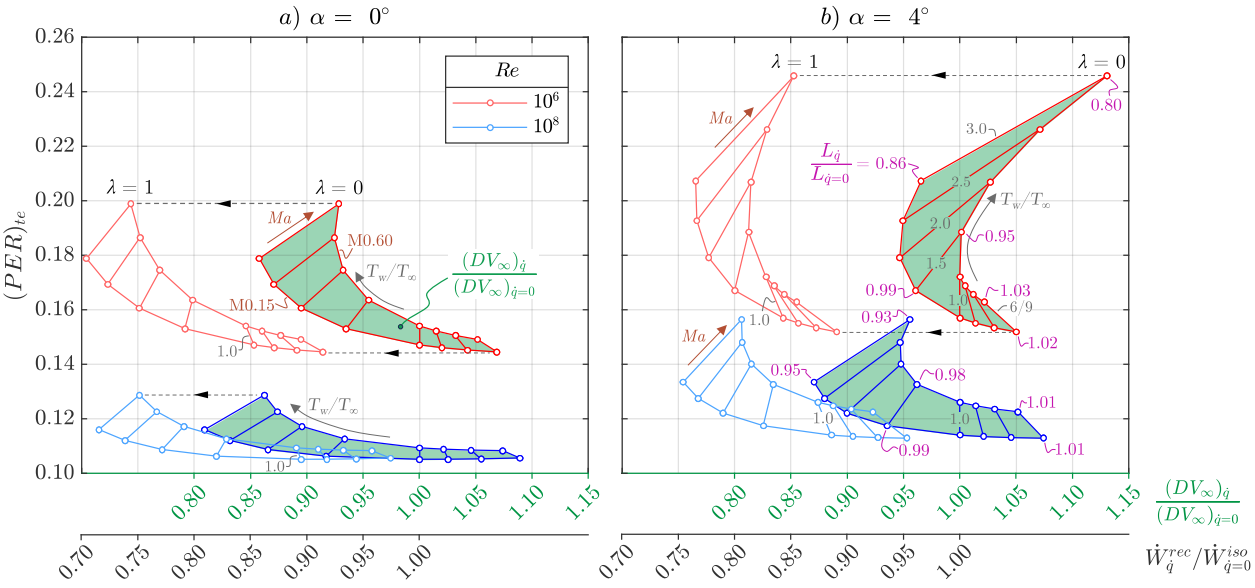

Fig. 20 Maps of non-adiabatic to adiabatic drag power ratio (shaded green), secondary x-axis showing maps (unshaded) of required propulsor work rate for zero and complete *PER* utilization.

[§§§] Analyses of wake ingesting propulsors typically assume the pressure field has recovered upstream of the propulsor inlet, $p_g \approx 0$.

[****] Axisymmetric fuselage or flat plate (adiabatic body) with a trailing edge actuator disc.

For $\lambda = 0$, $\dot{W}_{\dot{q}}^{rec}/\dot{W}_{\dot{q}=0}^{iso} = (DV_\infty)_{\dot{q}}/(DV_\infty)_{\dot{q}=0}^{iso}$ and the two maps coincide, though it is important to note that whilst these two ratios have the same value, they represent physically different quantities. This is made clear by increasing λ, which shifts the $\dot{W}_{\dot{q}}^{rec}/\dot{W}_{\dot{q}=0}^{iso}$ maps to the left, leaving the shaded $(DV_\infty)_{\dot{q}}^{rec}/(DV_\infty)_{\dot{q}=0}^{iso}$ map unchanged.

By using the adiabatic body in isolation as the baseline case, Fig. 20 highlights two opportunities for reducing $\dot{W}_{\dot{q}}^{rec}/\dot{W}_{\dot{q}=0}^{iso}$, the first being a direct reduction in the bodies drag power by surface heating, and the other by energy recovery. For the heated non-lifting case there is synergy, as DV_∞ is reduced and $(PER)_{te}$ is maximized, offering the greatest potential to reduce $\dot{W}_{\dot{q}}^{rec}/\dot{W}_{\dot{q}=0}^{iso}$. The lifting case ($\alpha = 4^\circ$) introduces two trade-offs, firstly there is a lift penalty associated with uniform surface heating[††††], and secondly, for the low Re_∞ high Ma_∞ map, $(PER)_{te}$ is maximized at the expense of increased DV_∞. However, depending on the value of λ, there could still be a reduction in $\dot{W}_{\dot{q}}^{rec}/\dot{W}_{\dot{q}=0}^{iso}$, suggesting that in some circumstances, localized heat rejection upstream of a BLI propulsor could be beneficial for performance, which is in agreement with Lamprakis et al. [22] work on axisymmetric fuselages. The lift penalty for uniform surface heating is, however, relatively insensitive to the high wall temperatures which have been simulated. For the extreme case, $\frac{T_w}{T_\infty} = 3.0$, the penalty is up to 20%, yet at more moderate temperature ratios such as $\frac{T_w}{T_\infty} \leq 1.5$ the lift penalty is up to 5%. Uniform surface heating was implemented in this work to study the influence on the flow field, but for future aircraft with waste heat to reject, localized heating is anticipated to be a more practical scenario through the integration of surface heat exchangers [9]. Strategic placement of these could provide a means to minimize the lift penalty or even increase lift [16], whilst enhancing the performance of wing integrated BLI propulsors through an increase in the potential for energy recovery.

V. Conclusion

A work-energy balance has been derived from the governing equations for a body in dynamic equilibrium moving through an initially quiescent atmosphere. This mechanical energy-based formulation, alongside the conventional near-field force equation, has been applied to an extensive test matrix of 2D RANS CFD cases of the NACA0012 airfoil. A range of freestream conditions have been examined for non-lifting and lifting scenarios with both adiabatic and non-adiabatic walls. The work-energy balance shows explicitly that the near-field work of the body manifests as global energy constituents, viscous dissipation and baroclinic work. The formulation enables the recoverable energy

[††††] Fig. 20 shows lift force ratios in magenta ref. from Fig. 13.

fraction, *PER*, to be calculated, and its application to an energy recovery device has been introduced in the context of wake and boundary layer ingestion using a *PER* utilization factor.

The analysis of a non-adiabatic body demonstrates that baroclinic losses can be significant even for low Mach numbers if heat sources or sinks are present, which is a direct result of non-isentropic expansion or contraction. The presence of strong thermal gradients reveals that *PER* is maximized by wall heating, as well as low *Re*, high α and high *Ma*, within the limits of stall and absent of shocks. These conditions reduce the fraction of total viscous losses that occur over the body, increasing *PER* at the trailing edge.

The increase in *PER* with wall heating, in some circumstances, such as lifting cases or low *Re*, comes at the expense of increased drag relative to an adiabatic case, due to the temperature gradients influence on the boundary layer, increasing its thickness and near wall curvature, pushing the flow towards separation. Despite this, a reduction in the required work rate supply from an on-board energy system may still be achieved, depending on the *PER* utilization factor of the aero-propulsive system. For a BLI system integrated into a lifting body, further consideration needs to be given as surface heating can introduce a lift penalty, potentially negating any benefits of increased *PER*. However, for uniform heating studied in this work, the lift penalty has been shown to be relatively insensitive for $T_w/T_\infty \leq 1.5$. Strategic local heating is a potential means to mitigate this penalty or even enhance lift.

Theoretically, heat sources and sinks could be used to optimize aerodynamic performance in flight. This isn't necessarily practical, but it does raise an interesting question regarding the best use of rejected of waste heat from battery-electric or fuel cell powered propulsion systems. Furthermore, localized heat rejection upstream of a BLI propulsor could enhance performance through a reduction in local mechanical energy dissipation. As a minimum, the flow physics should be understood to ensure that any aerodynamic penalties, if unavoidable, are at least accounted for during the systems level design stage of new aircraft.

Appendix

A. CFD Model Setup

The NACA0012 airfoil with a sharp trailing edge has been used throughout this work[‡‡‡‡]. It has simple, symmetric geometry and existing experimental and CFD results are well documented. All CFD work has been performed using

[‡‡‡‡] *https://turbmodels.larc.nasa.gov/naca0012numerics_val.html*

ANSYS FLUENT 2020 R2 and ICEM for meshing. Solutions were computed using the coupled solver, Green-Gauss cell-based gradient scheme with second order discretization and the *k-ω* SST turbulence model. Air was modelled as an ideal gas using Sutherland's equation for $\mu(T)$. c_p and k were assumed to be constant for the study of an adiabatic airfoil and equal to the freestream values listed in Table 3, whereas in the non-adiabatic study a piecewise polynomial and a kinetic theory-based equation were used for $c_p(T)$ and $k(T)$, respectively. Boundary conditions are depicted in Fig. 21.

Table 3 Freestream fluid properties

Property	Value	Unit
T_∞	300 K	K
a_∞	347.2	m/s
Pr_∞	0.737	-
γ_∞	1.4	-
$c_{p\infty}$	1006.82	J/kg/K
k_∞	1.846	W/m/K
μ_∞	0.0252	(10^{-5}) kg/m/s

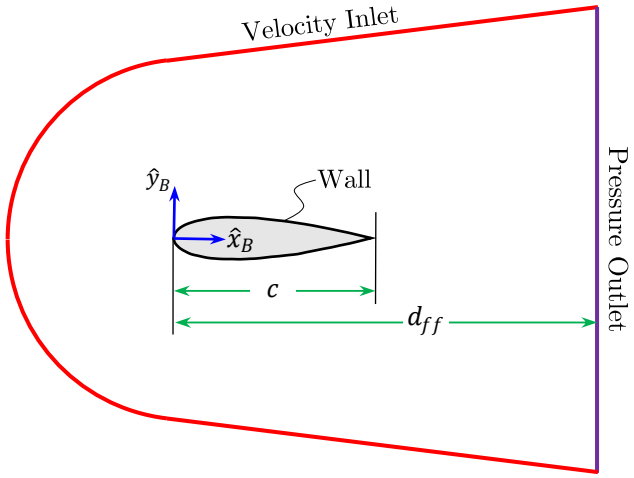

Fig. 21 CFD boundary conditions and domain shape, not to scale.

B. Mesh Refinement and Domain Size Study

A mesh refinement and domain size study for a single flow case has been performed following the method and nomenclature presented by ASME [42] . See Table 4 for detailed results. A total of nine meshes were produced, three domain sizes for three levels of mesh density, at *Re* = 6E+6, *Ma* = 0.15 and α = 10º. Normal to the wall a cell growth ratio of 1.05 was used, with the first cell height adjusted for each Reynolds number to ensure y^+ was less than, but

approximately equal to unity for all simulations. The distance from the leading edge to the pressure outlet (d_{ff}) in Fig. 21 is 300 chords for the final[§§§§] domain size.

Importantly, Fig. 22 shows that the solution has approached the asymptotic range, where C_{DV} is the drag power non-dimensionalized by $\frac{1}{2}\rho_\infty|\boldsymbol{V}_\infty|^3 S$. The error bars are within the Richardson's extrapolated solution. The values of GCI_{fine}^{21} are very low, almost less than 0.1% in all cases. Which means that no more than a 0.1% improvement to the results would be achieved with another refinement of the mesh for a refinement factor of $r \sim 1.3$. Also shown in Fig. 22 is a comparison of the drag power calculated using the work-energy balance and the drag power calculated using the near-field force integral. The two converged solutions match very well, which demonstrates that the work-energy balance theory discussed in section II has been applied correctly.

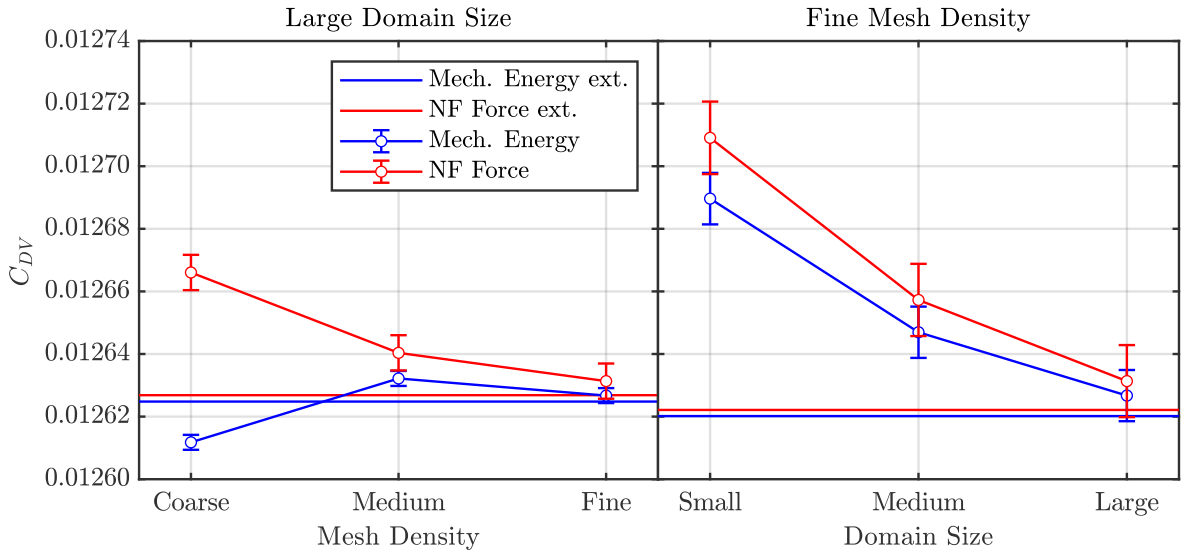

Fig. 22 Mesh convergence results, comparing near-field force and work-energy balance solutions, error bars show the convergence error index GCI_{fine}^{21}, horizontal lines depict Richardson's extrapolated values.

Furthermore, Table 5 compares near field force predictions from different CFD codes using the *k-ω* SST turbulence model with that of the mesh independent solution in Fig. 22. There is excellent agreement between the lift and drag coefficients. The data in Table 5 was collated by Jespersen et al. [43] from the NASA Langley turbulence modelling validation site for the NACA0012 airfoil[*****]. These results are well correlated against wind tunnel data, demonstrating that the flow is represented accurately by the RANS solution.

[§§§§] Corresponds to large domain size in Fig. 22.
[*****] https://turbmodels.larc.nasa.gov/naca0012_val_sst.html

Table 4 Drag power dependence on mesh density for three domain sizes using two drag power calculation methods for comparison: (a) Work-Energy balance, (b) Near Field Force

	Domain Size 1		Domain Size 2		Domain Size 3	
N_1	1,152,215		998,915		845,615	
N_2	648,249		556,349		464,449	
N_3	371,893		313,631		251,751	
	(a)	(b)	(a)	(b)	(a)	(b)
r_{21}	1.333	1.333	1.340	1.340	1.349	1.349
r_{32}	1.320	1.320	1.332	1.332	1.358	1.358
ϕ_1	0.012627	0.012631	0.012647	0.012657	0.012690	0.012709
ϕ_2	0.012632	0.012640	0.012648	0.012666	0.012691	0.012717
ϕ_3	0.012612	0.012666	0.012637	0.012691	0.012683	0.012741
Q	4.70	3.83	8.83	3.75	5.92	3.64
ϕ_{ext}^{21}	0.012625	0.012627	0.012647	0.012653	0.012689	0.012705
e_a^{21}	0.043%	0.072%	0.006%	0.069%	0.010%	0.062%
e_{ext}^{21}	0.015%	0.036%	0.001%	0.035%	0.002%	0.032%
GCI_{fine}^{21}	0.019%	0.045%	0.001%	0.043%	0.003%	0.040%

Table 5 Comparison of nearfield force predictions by different CFD codes using the k-ω SST turbulence model against the grid independent solution. Data extracted from ref. [43].

CFD Code	C_D	C_L
FLUENT (current paper)	0.01263	1.0767
CFL3D	0.01236	1.0778
FUN3D	0.01253	1.0840
NTS	0.01251	1.0765
OVERFLOW	0.01262	1.0847

Funding Sources

The authors received no financial support for the research, authorship, or publication of this article.

CRediT Author Statement

Joseph E. Lister-Symonds: Conceptualization, data curation, formal analysis, investigation, methodology, project administration, software, validation, visualization, Writing - original draft, review & editing. **Ngonidzashe E. Mutangara:** Conceptualization, review, software. **Ioannis Lamprakis:** Conceptualization, review. **Drewan S. Sanders:** Conceptualization, project administration, supervision, Writing – original draft, review & editing.

References

[1] A. Uranga, M. Drela, D. K. Hall and E. M. Greitzer, "Analysis of the Aerodynamic Benefit from Boundary Layer Ingestion for Transport Aircraft," *AIAA Journal,* vol. 56, no. 11, 2018, https://doi.org/10.2514/1.J056781.

[2] H. D. Kim, A. T. Perry and P. J. Ansell, "A Review of Distributed Electric Propulsion Concepts for Air Vehicle Technology," in *AIAA/IEEE Electric Aircraft Technologies Symposium*, Cincinnati, OH, 2018.

[3] N. G. Moirou, D. S. Sanders and P. Laskaridis, "Advancements and prospects of boundary layer ingestion propulsion concepts," *Progress in Aerospace Sciences,* vol. 138, 2023, https://doi.org/10.1016/j.paerosci.2023.100897.

[4] M. Drela, "Power Balance in Aerodynamic Flows," in *27th AIAA Applied Aerodynamics Conference*, San Antonio, TX, USA, 2009, https://doi.org/10.2514/1.42409.

[5] A. Arntz, O. Atinault and A. Merlen, "Exergy-Based Formulation for Aircraft Aeropropulsive Assessment: Theoretical Development," *AIAA Journal,* vol. 53, no. 6, pp. 1627-1639, 2015, https://doi.org/10.2514/1.J053467.

[6] M. Drela, "Considerations in Aerodynamic Force Decomposition," in *AIAA Aviation Forum*, Online, 2021, https://doi.org/10.2514/6.2021-2552.

[7] A. van Heerden, D. Judt, S. Jafari, C. Lawson, T. Nikolaidis and D. Bosak, "Aircraft thermal management: Practices, technology, system architectures, future challenges, and opportunities," *Progress in Aerospace Sciences,* vol. 128, 2022, https://doi.org/10.1016/j.paerosci.2021.100767.

[8] H. Kellermann, A. L. Habermann and M. Hornung, "Assessment of Aircraft Surface Heat Exchanger Potential," *MPDI Aerospace,* vol. 7, no. 1, 2020, https://doi.org/10.3390/aerospace7010001.

[9] A. L. Habermann, A. Khot, D. E. Lampl and C. Perren, "Aerodynamic Effects of a Wing Surface Heat Exchanger," *MPDI Aerospace,* vol. 10, no. 5, 2023, https://doi.org/10.3390/aerospace10050407.

[10] E. Reshotko, "Stability and Transition, How Much Do We Know?," in *Proceedings of the Tenth U.S. National Congress of Applied Mechanics*, New York, 1987.

[11] D. Mabey, "Effects of Heat Transfer on Aerodynamics and Possible Implications for Wind Tunnel Tests," *Prog. Aerospace Sci,* vol. 27, no. 4, pp. 267-303, 1990, https://doi.org/10.1016/0376-0421(90)90001-Z.

[12] C. J. Lin and R. L. Ash, "Wall Temperature Control of Low-Speed Body Drag," *Journal of Aircraft,* vol. 23, no. 1, 1986, https://doi.org/10.2514/3.45272.

[13] E. Reshotko, "Drag Reduction by Cooling in Hydrogen-Fueled Aircraft," *Journal of Aircraft,* vol. 16, no. 9, 1979, https://doi.org/10.2514/3.58571.

[14] B. R. Kramer, B. C. Smith and J. P. Held, "Drag Reduction Experiments Using Boundary Layer Heating," in *AIAA*, Reno, NV, USA, 1999, https://doi.org/10.2514/6.1999-134.

[15] A. Samiee, M. H. Djavareshkian, B. F. Feshalami and E. Esmaeilifar, "Improvement of Airfoils Aerodynamic Efficiency by Thermal Camber Phenomenon at Low Reynolds Number," *Journal of Aerospace Technology Mangement,* vol. 10, 2018, https://doi.org/10.5028/jatm.v10.954.

[16] H. Kallath, F. K. Kholi, M. Y. Ha, J. K. Min and J. Chetwynd-Chatwin, "Computational Study on the Aerodynamics of a Surface-Heated Wing for Thermal Management," *AIAA Journal,* vol. Article in advance, 2020, https://doi.org/10.2514/1.J059220.

[17] M. A. Aguirre and S. Duplaa, "Exergetic Drag Characteristic Curves," *AIAA Journal,* vol. 57, no. 7, 2019, https://doi.org/10.2514/1.J057985.

[18] A. Arntz, O. Atinault, D. Destarac and A. Merlen, "Exergy-based Aircraft Aeropropulsive Performance Assessment: CFD Application to Boundary Layer Ingestion," in *32nd AIAA Applied Aerodynamics Conference*, Atlanta, GA, 2014, https://doi.org/10.2514/6.2014-2573.

[19] D. S. Sanders and P. Laskaridis, "Full-Aircraft Energy-Based Force Decomposition Applied to Boundary-Layer Ingestion," *AIAA,* vol. 58, no. 10, pp. 4357-4373, 2020, https://doi.org/10.2514/1.J058695.

[20] N. E. Mutangara, L. Smith, K. J. Craig and D. S. Sanders, "Potential for Energy Recovery of Unpowered Configurations Using Power Balance Method Computations," *Journal of Aircraft,* vol. 58, no. 6, pp. 1364-1374, 2021, https://doi.org/10.2514/1.C036172.

[21] A. Arntz and O. Atinault, "Exergy-Based Performance Assessment of a Blended Wing–Body with Boundary-Layer Ingestion," *AIAA Journal,* vol. 53, no. 12, pp. 3766-3776, 2015, https://doi.org/10.2514/1.J054072.

[22] I. Lamprakis, D. S. Sanders and P. Laskaridis, "Energy-based Aerodynamic Loss and Recovery Characteristics of Adiabatic and Heated Fuselages," *Journal of Aircraft,* vol. 60, no. 6, pp. 1947-1964, 2023, https://doi.org/10.2514/1.C037246.

[23] I. Lamprakis, D. S. Sanders and P. Laskaridis, "Fundamental Concepts of Boundary Layer Ingestion," *Journal of Aircraft (Under Review),* 2024.

[24] A. J. Mallinckrodt and H. S. Leff, "All about work," *American Journal of Physics,* vol. 60, no. 4, pp. 356-365, 1992, https://doi.org/10.1119/1.16878.

[25] N. Renard and S. Deck, "A theoretical decomposition of mean skin friction generation into physical phenomena across the boundary layer," *Journal of Fluid Mechanics,* vol. 790, pp. 339-367, 2016, https://doi.org/10.1017/jfm.2016.12.

[26] D. S. Sanders, "Technical Report RP0028: Aircraft Aerodynamic Work-Energy Relationships with Mass Source Considerations," Cranfield University, Cranfield, UK, 2023.

[27] D. S. Sanders, "SUBLIME Deliverable 14 Report: Aircraft Level Assessment Including Uncertainty Propagation," Cranfield University, Cranfield, UK, 2023.

[28] I. Berhouni, D. Bailly and I. Petropoulos, "On the Definition of Exergy in the Field of Aerodynamics," *AIAA Journal,* vol. 61, no. 10, pp. 4356-4366, 2023, https://doi.org/10.2514/1.J062833.

[29] D. McLean, "Continuum Fluid Mechanics and the Navier-Stokes Equations," in *Understanding Aerodynamics*, Sussex, UK, John Wiley & Sons, 2013, https://doi.org/10.1002/9781118454190.ch3, pp. 13-74.

[30] S. Sato, "The Power Balance Method for Aerodynamic Performance Assessment," PhD Thesis, Department of Aeronautics and Astronautics, Massachusetts Institute of Technology, Cambridge, MA, 2012.

[31] I. Lamprakis, "Energy-based Aerodynamic Principles of Adiabatic and Heated Boundary Layer Ingestion," PhD Thesis, Cranfield University, Cranfield, UK, 2023.

[32] A. Uranga, M. Drela, E. M. Greitzer, D. K. Hall, N. A. Titchener, M. K. Lieu, N. M. Siu, C. Casses, A. C. Huang, G. M. Gatlin and J. A. Hannon, "Boundary Layer Ingestion Benefit of the D8 Transport Aircraft," *AIAA Journal,* vol. 55, no. 11, pp. 3693-3708, 2017, https://doi.org/10.2514/1.J055755.

[33] Y. A. Çengel and M. A. Boles, "Energy, Energy Transfer, and General Energy Analysis," in *Thermodynamics: An Engineering Approach*, New York, McGraw-Hill, 2015, ISBN 978-981-4595-29-2, pp. 51-110.

[34] F. M. White and J. Majdalani, Viscous Fluid Flow - 4th edition, New York, NY: McGraw-Hill, 2022, ISBN 978-1-260-59780-6.

[35] M. Drela, "Aerodynamics of Aircraft in Maneuver," in *Flight Vehicle Aerodynamics*, Cambridge, MA, The MIT Press, 2014, ISBN 9780262319928, pp. 123-142.

[36] M. Drela, "Physics of Aerodynamic Flows," in *Flight Vehicle Aerodynamics*, Cambridge, MA, The MIT Press, 2014, ISBN 9780262319928, pp. 1-21.

[37] D. McLean, "Lift and Airfoils in 2D at Subsonic Speeds," in *Understanding Aerodynamics*, Sussex, UK, John Wiley & Sons, 2013, https://doi.org/10.1002/9781118454190.ch7, pp. 259-354.

[38] D. McLean, "Aerodynamic Lift," *The Physics Teacher,* vol. 56, no. 8, pp. 516-520, 2018, https://doi.org/10.1119/1.5064558.

[39] P. Lissaman, "The facts of lift," in *AIAA, 34th Aerospace Sciences Meeting and Exhibit*, Reno, NV, 1996, https://doi.org/10.2514/6.1996-161.

[40] D. K. Hall, A. C. Huang, A. Uranga, E. M. Greitzer, M. Drela and S. Sato, "Boundary Layer Ingestion Propulsion Benefit for Transport Aircraft," *Journal of Propulsion and Power,* vol. 33, no. 5, pp. 1118-1129, 2017, https://doi.org/10.2514/1.B36321.

[41] P. Lv, A. G. Rao, D. Ragni and L. Veldhuis, "Performance Analysis of Wake and Boundary-Layer Ingestion for Aircraft Design," *Journal of Aircraft,* vol. 53, no. 5, pp. 1517-1526, 2016, https://doi.org/10.2514/1.C033395.

[42] ASME, "Procedure for Estimation and Reporting of Uncertainty Due to Discretization in CFD Applications," *Journal of Fluids Engineering,* vol. 130, no. 7, 2008, https://doi.org/10.1115/1.2960953.

[43] D. C. Jespersen, T. H. Pulliam and M. L. Childs, "OVERFLOW Turbulence Modeling Resource Validation Results," NASA Ames Research Center, Moffett Field, CA, 2016, https://turbmodels.larc.nasa.gov/Papers/NAS_Technical_Report_NAS-2016-01.pdf.

Potential for energy recovery of a nonadiabatic subsonic airfoil

Lister-Symonds, Joseph E.

2025

Lister-Symonds JE, Mutangara NE, Lamprakis I, Sanders DS. (2025) Potential for energy recovery of a nonadiabatic subsonic airfoil. Journal of Aircraft, Available online 13 February 2025
https://doi.org/10.2514/1.c037894